Sedimentary pyrite as a gold-source in sediment-hosted gold occurrences in the Selwyn basin area, eastern Yukon

Patrick J. Sack[1]
Yukon Geological Survey

L.V. Danyushevsky, R.R. Large, S. Gilbert, and D. Gregory
CODES, ARC Centre of Excellence in Ore Deposits, University of Tasmania, Australia

Sack, P.J., Danyushevsky, L.V., Large, R.R., Gilbert, S., and Gregory, D., 2014. Sedimentary pyrite as a gold-source in sediment-hosted gold occurrences in the Selwyn basin area, eastern Yukon. *In:* Yukon Exploration and Geology 2013, K.E. MacFarlane, M.G. Nordling, and P.J. Sack (eds.), Yukon Geological Survey, p. 195-220.

ABSTRACT

Intrabasinal sedimentary pyrite has recently been proposed as a potential gold source for sediment-hosted gold deposits. To evaluate this concept in the Selwyn basin area of eastern Yukon, we use laser ablation-inductively coupled plasma-mass spectrometry (LA-ICP-MS) to analyse pyrite from the Carlin-type Conrad, and orogenic gold 3Ace occurrences. This paper texturally and chemically characterizes four generations of pyrite in grey to black mudstones and siltstones, but focuses 83% of the analyses on early and late diagenetic pyrite. Diagenetic pyrite from the Conrad occurrence is trace element poor with respect to deposit-proximal pyrite from shales in the Northern Carlin Trend of Nevada, but is similar in composition to distal diagenetic pyrite in these Nevada shales. Diagenetic pyrite from the 3Ace occurrence is very similar in composition to pyrite around the giant Sukhoi Log deposit in eastern Russia. It can be preliminarily concluded that the trace element composition of diagenetic pyrite from the Conrad and 3Ace occurrences is permissive of a locally derived intrabasinal sedimentary pyrite gold source.

[1] *patrick.sack@gov.yk.ca*

INTRODUCTION

The Selwyn basin area of eastern Yukon has seen significant discoveries of sediment-hosted gold (*i.e.*, Carlin-type and orogenic gold deposit styles) in recent years. Carlin-type gold was discovered in 2010 on the northern margin of the Selwyn basin area (*e.g.*, Tucker *et al.*, 2013), and a recent review of these occurrences indicates they share many similarities with deposits found in Nevada (Arehart *et al.*, 2013). 3Ace, an orogenic gold occurrence in the SE part of the basin (Hart and Lewis, 2006), is another of these discoveries, returning multi-gram gold intercepts (*e.g.*, Northern Tiger Resources, October 25, 2011 news release). These recent gold discoveries mark newly identified metallogenic events for the Selwyn basin area, an area historically known for sedimentary exhalative (SEDEX) base metal deposits (Goodfellow, 2007). Most of what is known about the Selwyn basin area comes from the base metal exploration boom between the mid-1970's and early-1990's (*e.g.*, Abbott *et al.*, 1990; Goodfellow *et al.*, 1995; Goodfellow and Jonasson, 1987; Gordey and Anderson, 1993; Lydon *et al.*, 1979; Pigage, 1990). The notable exception to this is work done on reduced intrusion related gold systems in the northwest portion of the Selwyn basin area (*e.g.*, Hart, 2007; Lang and Baker, 2001). Another phase of research in Selwyn basin area geology is underway with the recent gold discoveries stimulating regional mapping (Chakungal and Bennett, 2011; Colpron, 2012; Colpron *et al.*, 2013; Moynihan, 2013) (Moynihan, 2014)and deposit research (Arehart *et al.*, 2013; Sack *et al.*, 2013; Tucker *et al.*, 2013; Whelan *et al.*, 2013).

Concurrent with, and slightly preceding, the recent surge in sediment-hosted gold exploration interest in the Selwyn basin area, have been technical advances in micro-analytical techniques allowing higher quality, faster, and less expensive studies of mineral chemistry, specifically on sulphides such as pyrite. Mineral petrogenesis coupled with laser ablation-inductively coupled plasma-mass spectrometer (LA-ICP-MS) pyrite studies have led to a new source-rock model using sedimentary pyrite, in local carbonaceous sedimentary rocks, as a gold, and associated trace element, source for sediment-hosted gold deposits (Large *et al.*, 2011). This model has subsequently been supported by fluid inclusion data (Gaboury, 2013), as well as additional pyrite chemistry data from other gold systems (*e.g.*, Large *et al.*, 2012). From a regional exploration perspective, this model is significant because it posits that regionally extensive sedimentary rocks, which host gold deposits, are likely to be the source of gold for these deposits. Furthermore, given that gold in these rocks is dominantly within pyrite, analyses of the sedimentary pyrite from intrabasinal strata may allow evaluation of the gold fertility of a basin. This is much different than most accepted sediment-hosted gold models that source gold from outside the basin (*e.g.*, metamorphic and/or magmatic fluids, Cline *et al.*, 2005; far travelled metamorphic fluids, Groves *et al.*, 1998). If this new model is correct, it potentially provides a powerful, first order discriminant of sedimentary basin (or specific strata within a basin) gold productivity, that is, does the sedimentary pyrite contain enough gold to produce economic sediment-hosted gold deposits? In this paper, we characterize predominantly sedimentary pyrite from two sediment-hosted gold occurrences in the Selwyn basin area, and compare these data against published pyrite data from near analogue deposits.

STUDY LOCATIONS

To investigate the potential of sedimentary pyrite as a gold-source in the Selwyn basin area, we sampled diamond drill core from two of the better known sediment-hosted gold occurrences, the Carlin-type Conrad occurrence (Tucker *et al.*, 2013) and the orogenic gold 3Ace occurrence (Hart and Lewis, 2006; Fig. 1). Neither occurrence has a defined resource, and only preliminary research has been completed (*e.g.*, Sack *et al.*, 2013; Tucker *et al.*, 2013; Whelan *et al.*, 2013), but both have been diamond drilled and a simple geological characterization of them is possible. A preliminary comparison between the Yukon Carlin-type occurrences (*e.g.*, Osiris, Conrad, and Isis) and the Carlin-type deposits in Nevada determined that they share many similarities, however more detailed research on the Yukon occurrences is needed (Arehart *et al.*, 2013). The main difference noted was the lack of Tertiary extension and magmatism near the Yukon examples (Arehart *et al.*, 2013). Initial work on the Conrad occurrence has demonstrated drill intercepts in the 1 g/t to 10 g/t Au range over 10's of metres, with the best intercept to date being 42.93 m of 18.44 g/t Au; including 16.73 m of 30.85 g/t Au (J. Lane, written comm.), which is comparable to the grade of Carlin-type deposits in Nevada (Cline *et al.*, 2005).

The 3Ace occurrence is found within the southeastern portion of the Tintina Gold Belt (Hart *et al.*, 2002), and was originally thought to be intrusion-related in origin, but a preliminary review of occurrences in the area by Hart and Lewis (2006) determined that the 3Ace occurrence shares more similarities with the orogenic gold deposit

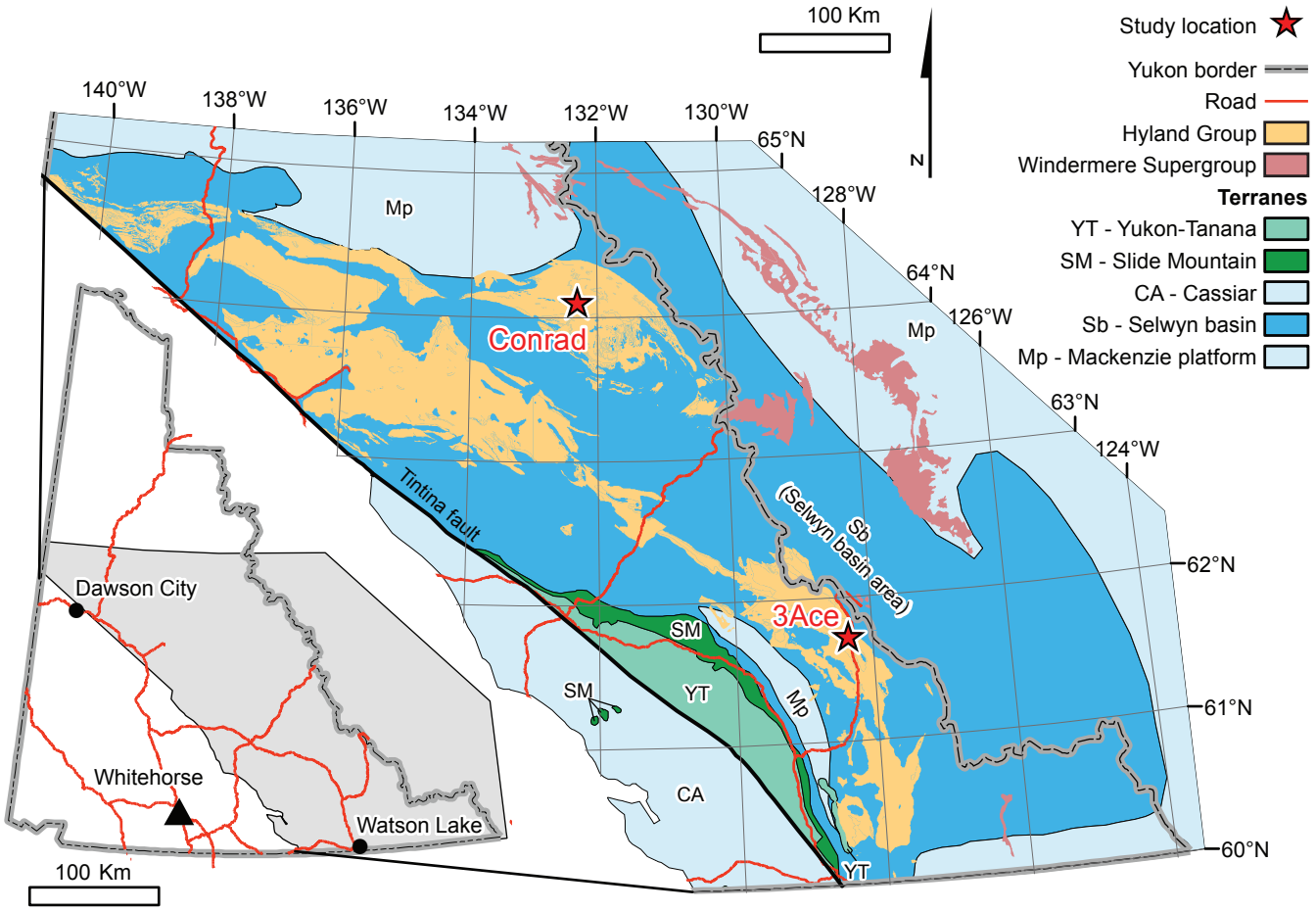

Figure 1. *Generalized geological map showing extent of the Selwyn basin area and distribution of Neoproterozoic strata in the northern Canadian Cordillera. The regional distribution of Windermere Supergroup is from Wheeler and McFeely (1991), and Hyland Group is from Gordey and Makepeace (2001). Note that the Conrad occurrence is shown as being hosted within the Hyland Group, but recent mapping by Colpron et al. (2013) places it within the Windermere Supergroup. Inset at bottom left shows extent of this map with respect to the Yukon Territory.*

style. The nearby Justin property, approximately 5 km to the east, has potential intrusion-related gold mineralization and preliminary fluid inclusion data on the Main Zone vein at the 3Ace are permissive of either magmatic or metamorphic fluid sources (Whelan *et al.*, 2013). Orogenic gold deposits tend to have a slightly higher, but less consistent, Au grade compared to Carlin-type deposits, with orogenic grades typically ranging from 3 g/t to 15 g/t Au (Goldfarb *et al.*, 2005). The best intercept, to date, from the 3Ace occurrence is 4.6 g/t Au over 35 m with several other intercepts between 1.4 g/t and 3.8 g/t Au over 10s of metres (Northern Tiger Resources, September 26 and October 25, 2011 news releases), similar in grade to known orogenic gold deposits. Both occurrences have mineralized diamond drill intercepts over several hundreds of metres of strike length and intercept grades comparable to known deposit grades. From the point of view of this study, the Conrad occurrence is a reasonable example of Carlin-type mineralization (Tucker *et al.*, 2013) and the 3Ace occurrence of orogenic gold mineralization (Hart and Lewis, 2006); where they sit exactly in their respective deposit-type spectrums is not currently known.

REGIONAL GEOLOGY

Eastern Yukon, north of the Tintina fault, is primarily made up of sedimentary and minor volcanic rocks of western Laurentian affinity that are Paleoproterozoic and younger (Nelson *et al.*, 2013). In broad terms, these can be divided into a 'basement', composed of rocks approximately

1.6 Ga to 0.78 Ga, and overlying Neoproterozoic–Paleozoic basinal sedimentary rocks (Gordey and Anderson, 1993; Fig. 2). The oldest of the 'basement' rocks, the 1.64 Ga to 1.60 Ga Wernecke Supergroup, comprises a sequence of sedimentary rocks that were deposited in a broadly subsiding marine basin, presumably floored by crystalline basement (Thorkelson *et al.*, 2001). These are intruded, and overlain by, mafic volcanic rocks of the Hart River sills and basalts (Abbott, 1997). Siliciclastic and carbonate rocks of the Pinguicula Group were deposited unconformably on the Hart River basalts in a slope to basin environment, and preliminary detrital zircon data suggest they are younger than approximately 1.15 Ga (Medig *et al.*, 2012). The youngest 'basement' rocks are the Mackenzie Mountain Supergroup, a thick succession of shallow marine limestone, evaporite, and fluvial sedimentary rocks deposited in an extensional basin, possibly as an early product of the breakup of Rodinia (Turner and Long, 2008). Collectively, these four units make up the 'basement' for post-0.78 Ga rift-related sedimentary rocks belonging to the Windermere Supergroup (Abbott, 1997; Eisbacher, 1981), the uppermost strata of which is broadly time-equivalent with the lowermost Selwyn basin stratigraphy, the Hyland Group (Moynihan, 2014).

SELWYN BASIN AREA

The term 'Selwyn basin' has seen several uses since its creation by Gabrielse (1967), and is thoroughly discussed in Gordey and Anderson (1993). The commonly accepted definition of Gordey and Anderson (1993, p. 14-15) which defines Selwyn basin as *"a region of deeper water offshelf sedimentation that persisted from the late Precambrian to Middle Devonian"* is used in this study. In the study area, the late Precambrian Hyland Group through to the Ordovician-Devonian Road River Group make up the basin stratigraphy; the overlying Devono-Mississippian Earn Group is not part of the basin stratigraphy (Gordey and Anderson, 1993). Though the upper Windermere Supergroup and lower Hyland Group are broadly age-equivalent, the majority of Windermere rocks are much older and thus not part of Selwyn basin (Moynihan, this volume). When referring to the geographical area roughly delineated by the Paleozoic carbonate-shale boundary, an area that includes both Windermere Supergroup and Hyland Group rocks, the term Selwyn basin area is used, as outlined in Figure 1.

The recently discovered, disseminated, Carlin-type gold occurrences (*e.g.*, Conrad, Osiris, and Isis zones) are predominantly found in fine-grained siliciclastic and carbonate rocks of the Neoproterozoic Windermere Supergroup, in the eastern part of the Rackla belt, north of the Dawson fault (Figs. 1 and 2; Colpron *et al.*, 2013; Tucker *et al.*, 2013). This belt straddles the Dawson fault, which defines the northern margin of Selwyn basin (Abbott, 1997). To the south of the Dawson fault, hanging wall stratigraphy consists of coarse-grained Hyland Group rocks, unconformably overlain by fine-grained Earn Group shale, chert, and sandstone, which are capped by Carboniferous to Triassic strata (Colpron *et al.*, 2013). Stratigraphy of the upper Windermere Supergroup in the footwall, to the north of the Dawson

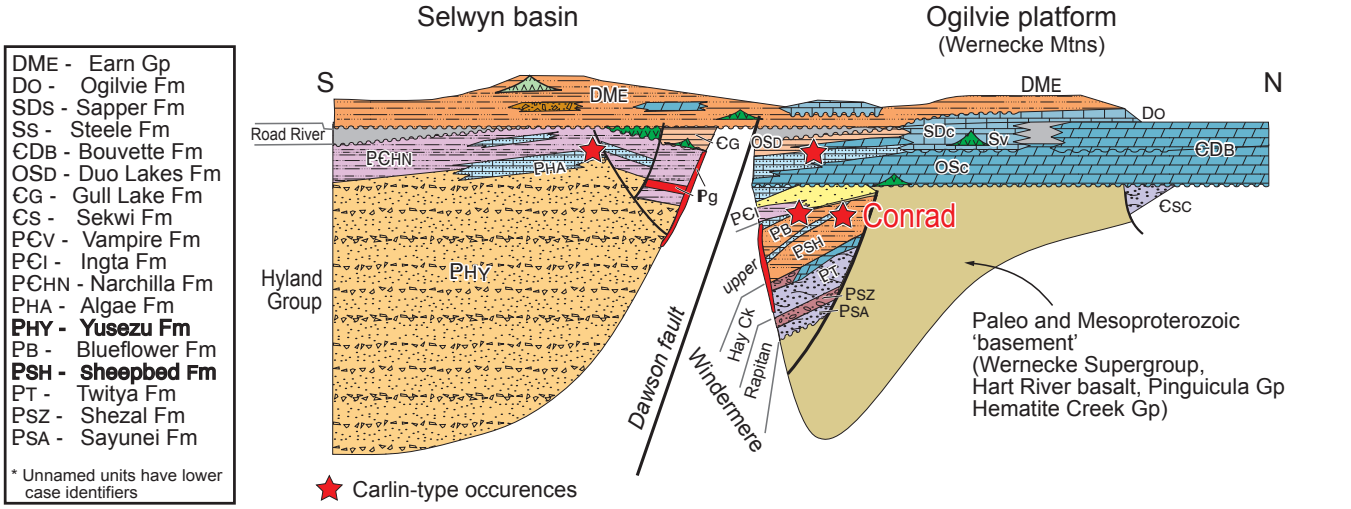

Figure 2. *Schematic north-south cross-section of the study area near the Conrad occurrence in east-central Yukon showing stratigraphic relationships for Neoproterozoic and younger strata of the Ancestral North American margin from Nelson et al. (2013) after Abbott (1997).*

fault, is generally correlative, but of very different facies (Colpron *et al.*, 2013). These upper Windermere rocks in the Rackla belt are slope deposits and lateral facies variations of Windermere Supergroup, as seen in the Wernecke Mountains and Mackenzie Mountains to the north (Colpron *et al.*, 2013). These upper Windermere slope deposits pass southward into deeper-water basinal deposits of the Hyland Group (Yusezyu Formation) (Moynihan, 2014). The regional metamorphic grade of the rocks in the Rackla belt is prehnite-pumpellyite (Read *et al.*, 1991).

The 3Ace occurrence is located in the upper Hyland River valley of eastern Yukon (Hart and Lewis, 2006; Whelan *et al.*, 2013; Fig. 1), an area of poorly understood regional geology that was last mapped in the 1960's (Blusson, 1966). The most recent regional mapping nearby is NTS map sheet 105I, the map sheet directly to the north of the 3Ace occurrence (Gordey and Anderson, 1993). The 3Ace occurrence is hosted by quartz veins best developed in coarse-grained sandstone of the Yusezyu Formation of the Hyland Group. Regionally, the Hyland Group is characterized by coarse-grained siliciclastic rocks (Yusezyu Formation), overlain by a thin discontinuous limestone (Algae Formation), and capped by maroon and green shale (Narchilla Formation) (Cecile, 2000; Gordey and Anderson, 1993). Approximately 5 km to the northeast of the 3Ace occurrence is the March fault, a fundamental geologic structure that separates Hyland Group basinal facies rocks from slope facies rocks of the Vampire Formation (Gordey and Anderson, 1993; Fig. 3). This thrust fault may be southwest dipping, and likely began life as a synsedimentary Neoproterozoic structure, possibly a normal fault, which controlled regional facies distributions until at least the early-Cambrian; it was later reactivated as a thrust fault during regional Cretaceous deformation (Gordey and Anderson, 1993; Hart and Lewis, 2006). The regional metamorphic grade of rocks in the Hyland River valley area is sub-greenschist to lower greenschist facies (chlorite zone); rocks directly adjacent to intrusions have been contact metamorphosed up to amphibolite facies (Moynihan, 2013; Read *et al.*, 1991).

PROPERTY-SCALE GEOLOGY

CONRAD OCCURRENCE

The Conrad deposit is hosted by a limestone unit which cores a doubly plunging antiform trending north-northeast (Tucker *et al.*, 2013). This limestone unit is found within a southward-younging sedimentary package that can be divided into lower stratigraphy, that hosts the Conrad occurrence (Nadaleen formation), and upper stratigraphy, which hosts the Osiris occurrence (Gametrail Formation; Colpron *et al.*, 2013). In the vicinity of the Conrad occurrence, the Nadaleen formation consists of silty limestone with siltstone and sandstone as well as large carbonate debris flows interbedded with black shale and siltstone, all overlain by maroon and green siltstone (Tucker *et al.*, 2013). Locally, the Gametrail Formation consists of a main limestone package, capped by a sequence of silty limestone and siltstone, diamictite, and dolomite (Tucker *et al.*, 2013).

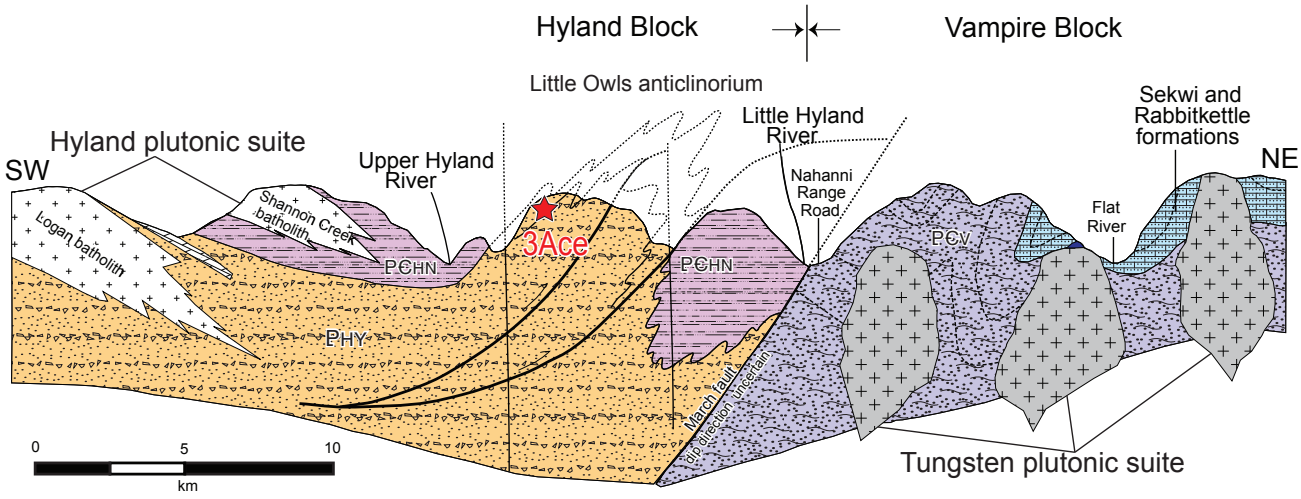

Figure 3. *Northeast-southwest schematic structural section of the upper Hyland River valley area (modified from Hart and Lewis, 2006); 3Ace occurrence projected approximately 20 km from the southeast. Unit abbreviations same as Figure 2.*

SUMMARY OF DIAMOND DRILL CORE LOGGING

Detailed logging of the mudstone-siltstone dominated intervals from two diamond drill holes into the Conrad occurrence was done in July 2012. Diamond drill hole OS11-74 is located in the middle of the Conrad occurrence with the best gold intersection starting at 245.97 m and consisting of 33.11 m of 2.67 g/t Au (ATAC Resources, November 23, 2011 news release). Diamond drill hole OS11-70 is located approximately 300 m west, on the western flank of the occurrence with several gold intersections (Fig. 4), the best of which is 15.24 m of 7.51 g/t Au starting at 243.84 m (ATAC Resources, November 23, 2011 news release).

Diamond drill hole OS11-74 has core recovery starting at 3.2 m depth and the hole ending at 639.17 m, but is heavily faulted in the upper 92 m; the interval from 3.2 m to 248.72 m was logged for this study and is shown graphically in Figure 4. The interval from 3.2 m to 25.47 m consists of a heavily faulted dark brown to black limestone breccia with a calcareous matrix, from 25.47 m to 92.0 m is also heavily faulted but with short (<2 m) unfaulted sections, the core is dominantly thinly laminated, dark grey to black, very fine-grained sandstone and siltstone with variable carbonate content (Fig. 5). The interval from 92.0 m to 102.0 m consists of dolomite with realgar and orpiment veins. From 102.0 m to 155.83 m are a series of thin (1-3 m) normally graded, polymictic pebble to coarse

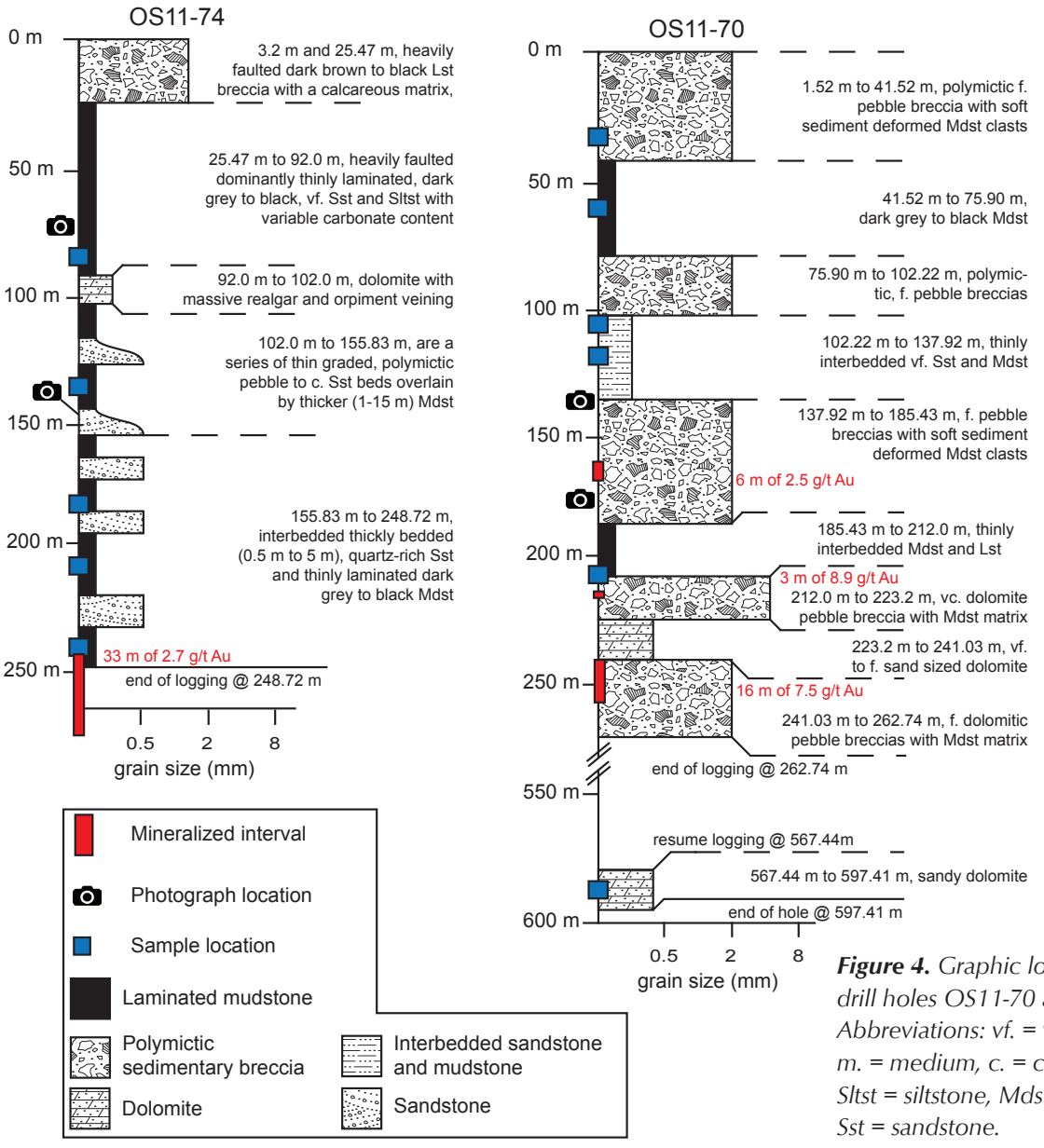

Figure 4. *Graphic logs of diamond drill holes OS11-70 and OS11-74. Abbreviations: vf. = very fine, f. = fine, m. = medium, c. = coarse; Lst = limestone, Sltst = siltstone, Mdst = mudstone, Sst = sandstone.*

sandstone beds overlain by thick intervals (1-15 m) of thinly laminated mudstone that is variably calcareous. The interval from 155.83 m to 248.72 m (end of logging) is made up of thickly bedded (0.5 m to 5 m), coarse-grained quartz sandstone interbedded with thinly laminated dark grey to black mudstone (Fig. 5). Sandstone-dominated intervals vary from 1 m to 10 m in apparent thickness and mudstone-dominated intervals are slightly thicker, varying between 1 m and 15 m.

Diamond drill hole OS11-70 is 597.41 m long with recovery starting at 1.52 m; 1.52 m to 262.74 m and 567.44 m to 597.41 m were logged for this study and are shown graphically in Figure 4. The core in this hole is less faulted than that in OS11-74, but does have short (<1 m to 10 m) faulted intervals. The interval from 1.52 m to 41.52 m is a weakly stratified to unstratified, poorly sorted, polymictic fine pebble breccia with soft sediment deformed mudstone clasts, white quartz clasts, light grey dolomite clasts and pale green mudstone clasts. The pale green clasts are likely of upper Nadaleen formation origin. Within this interval are several interlaminated mudstone and sandstone sequences up to 8 m in apparent thickness, some with highly irregular and contorted bedding suggesting soft sediment deformation. The interval from 41.52 m to 75.90 m is dominantly dark grey to black mudstone but includes thin dolomitic beds from 53.15 m to 59.0 m and complex, soft sediment deformed beds between 59.0 m and 75.90 m; the upper 11.63 m is intensely faulted. Between 75.90 m and 102.22 m, are normally graded, polymictic, fine pebble breccias with angular to subrounded limestone clasts and minor black mudstone clasts. Several short intervals within these breccias are intensely altered, displaying noticeable decalcification and minor realgar (Fig. 5). The interval between 102.22 m and 137.92 m is dominated by thinly interbedded very fine-grained sandstone and mudstone that is weakly dolomitic; some mudstone sections show evidence of both brittle and ductile (soft sediment) deformation. From 137.92 m to 185.43 m are several thick (up to 20 m) horizons of normal and reverse graded, fine pebble breccias with soft sediment deformed mudstone clasts (Fig. 5). The interval between 185.43 m and 212.0 m is thinly interbedded mudstone and limestone with faulted intervals from 185.43 m to 193.0 m and 198.12 to 206.0 m. The interval from 212.0 m to 223.2 m is a reversely graded, very coarse dolomitic pebble breccia with a mudstone matrix. From 223.2 m to 241.03 m is a very fine to fine-grained, weakly bedded dolomite. The interval from 241.03 m to 262.74 m (end of continuous logging) consists of several fine dolomitic pebble breccias with white quartz and dolomitic clasts within a dolomitic mudstone matrix; the breccias are separated by very fine grained dolomite intervals <5 m in apparent thickness. The interval at the bottom of the hole, 567.44 m to 597.41 m, is composed of weakly bedded fine to medium-grained dolomite including two reversely graded and one normally graded, coarse sandstone to fine pebble conglomerate beds approximately 75 cm thick.

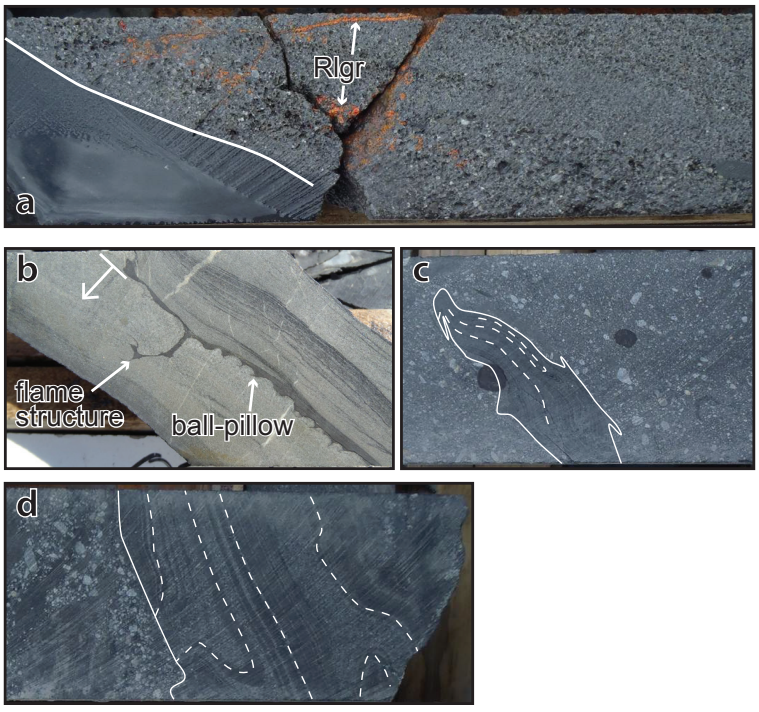

Figure 5. *Representative rocks from the Conrad occurrence, location of photos shown on Figure 4. (a) OS11-74 at 76.90 m: decalcified and silicified fine pebble conglomerate with realgar (Rlgr) in veins and on fractures. (b) OS11-74 at 146.70 m: load structures in fine sandstone and mudstone, way-up indicated by flat-bottomed arrow. (c) OS11-70 at 177.66 m: deformed mudstone clast (outlined in solid white) within pebble conglomerate. (d) OS11-70 at 139.0 m: base of a fine pebble conglomerate bed eroding complexly deformed, siltstone-mudstone beds. All photos of NQ diamond drill core; approximately 5 cm in diameter.*

The abundance of coarse-grained, graded beds and polymictic, pebble breccias with soft sediment deformed, mudstone clasts are interpreted as slump or debris flow deposits. Intervening periods of quiet water sedimentation were deposited as the thicker mudstone sequences. These interpretations are consistent with an overall slope, or near slope depositional environment as suggested by other researchers (*e.g.*, Arehart *et al.*, 2013; Colpron *et al.*, 2013; Tucker *et al.*, 2013).

3ACE OCCURRENCE

Property-scale mapping (1:10 000) at the 3Ace occurrence has documented a series of imbricated, north-dipping, thrust stacks of Hyland Group rocks (Buchanan and Oullette, 2013). Most of the mapped lithologies are consistent with the Yusezyu Formation as described by Gordey and Anderson (1993). At 3Ace the Yusezyu Formation consists of coarse-grained, arkosic sandstone and coarse to medium-grained quartz pebble conglomerate containing approximately 30% black and grey phyllites (Buchanan and Oullette, 2013). Near the northern limit of property mapping, and continuing further north, a series of calcareous lithologies have been tentatively correlated with the Algae Formation (Buchanan and Oullette, 2013), as noted elsewhere, stratigraphically above the Yusezyu Formation (*e.g.*, Cecile, 2000; Colpron, 2012; Colpron *et al.*, 2013). The lower greenschist (chlorite zone) regional metamorphism (Read *et al.*, 1991) has not recrystallized the rocks and is best seen in the fine-grained, carbonaceous, siliciclastic-dominated intervals that are now fine-grained, carbonaceous, black phyllites; sedimentary features such as grain size, bedding, grading, and load structures are easily recognizable. Due to the generally intimate laminations between mudstone and very fine-grained sandstone in the carbonaceous phyllite intervals, the overall low metamorphic grade, and the easily seen sedimentary structures, the terms mudstone and sandstone are used as opposed to phyllite to emphasize the protolith grain size difference; it is recognized that the rocks are weakly metamorphosed. Two sets of strike-slip faults cross-cut the stratigraphy; the Main Zone, where the holes used in this study were drilled, is along a north-striking fault. There are several east-striking faults on the property as well.

SUMMARY OF DIAMOND DRILL CORE LOGGING

Five hundred and ninety-one metres of core from two holes into the Main Zone at Northern Tiger Resources' 3Ace property were logged in late July and early August 2012. Diamond drill hole 3A11-15A is located in the centre of the Main Zone with the best gold intersection being 2.51 g/t Au over 27.2 m, starting at 83.30 m depth (Northern Tiger Resources, October 25, 2011 news release). Diamond drill hole 3A11-24A was collared 139 m to the south and did not intersect significant amounts of gold.

Diamond drill hole 3A11-15A, is 386.0 m long with recovery starting at a depth of 3.0 m; the entire hole was logged for this study and is shown graphically in Figure 6. The top interval from 3.0 m to 83.50 m is dominantly (~75%) very fine sandstone and lesser (~25%) interbedded mudstone. The sandstone is medium grey and thickly laminated to thinly bedded, with bed thicknesses ranging from 5 mm to 50 mm; the mudstone is black and thinly laminated, with bed thicknesses between 1 mm and 5 mm. The interval from 83.50 m to 103.10 m contains the best gold grades in the hole and is predominantly made up of massive, medium to coarse-grained sandstone with Au carried in cross-cutting, white quartz veins (Fig. 7); the upper approximately 3 m is a fine pebble, clast-supported conglomerate fining downhole into coarse-grained sandstone. The interval from 103.10 m to 257.72 m consists of alternating intervals (10-30 m) of coarse-grained sandstone to fine pebble conglomerate, and thinly laminated very fine sandstone and mudstone. Contacts between the fine and coarse-grained lithologies typically show depositional features such as loading (Fig. 7). The interval from 257.72 m to 343.50 m is a series of thick (0.5-7 m), normally graded beds with intervals (10 m or less) of medium to coarse-grained quartz sandstone. The remaining interval from 343.50 m to 386.0 m (end of hole) is heavily faulted, thinly interlaminated mudstone and medium-grained sandstone.

Diamond drill hole 3A11-24A was drilled to a depth of 205.0 m with recovery starting at 10.5 m. The interval between 10.50 m and 141.65 m is made up of alternating, thick sections (5-15 m) of dark grey to black, interbedded fine-grained sandstone and mudstone, and medium grey, coarse-grained, graded, and thickly bedded to massive quartz sandstone (Fig. 7). A bottom interval between 141.65 m and 205.0 m (end of hole) is composed of black, laminated mudstone (~90%) and very fine-grained dark grey sandstone (~10%).

Both holes logged from the 3Ace occurrence contain abundant, thick (up to 30 m) intervals of thickly-bedded to massive, coarse-grained sandstone (*e.g.*, 3A11-15A, 103.10 m to 257.72 m). There are also thick intervals of

fine-grained siliciclastic rocks (*e.g.*, 3A11-24A, 141.65 m to 205.0 m). The coarse grain size and thick-bedded nature of these rocks suggest they were deposited proximal to their source. This is consistent with deposition in submarine fan deposits proximal to the basin margin, but within the basin proper, as suggested by previous researchers (Gordey and Anderson, 1993; Hart and Lewis, 2006).

LA-ICP-MS ANALYTICAL METHODS

Two types of laser ablation-inductively coupled-mass spectrometer (LA-ICP-MS) instruments were used in this study to obtain quantitative spot data and semi-quantitative element image maps. These data were determined using a New Wave UP-213 Nd:YAG Laser Ablation System, coupled with either an Agilent 7500a ICP-QMS or an Agilent 7700s ICP-MS at the ARC Centre of Excellence in Ore Deposits at the University of Tasmania. The choice of ICP-MS was determined by availability, however both generated comparable datasets. Depending on the size of pyrite being ablated, the beam diameter was between 20 µm and 50 µm with most of the analyses done at 31 µm and 35 µm. All ablation was completed in an ultra-high purity He atmosphere, and the resulting aerosol was mixed with an Ar carrier gas before introduction to the ICP-MS. Laser energy of ~3.5 J cm^{-2} and a repetition rate of 5 Hz were used for all analyses. Data was collected over 70-90 s intervals, with a 30 s pre-ablation acquisition (background) interval and a 40-60 s acquisition interval. Generally 20 s of the laser-on data, equivalent to approximately 10 µm depth using a penetration rate of 0.5 µm/s, was used for data reduction. In most cases this was sufficient time to produce analyses with adequate detection limits (Table 1). However in the case of thin hydrothermal rims observed at the Conrad occurrence (1 µm to 5 µm; Tucker *et al.*, 2013), only seven analyses of rims were obtained.

Semi-quantitative element maps of pyrite were collected with the same analytical set-up as spot acquisition but using the technique described by Large *et al.* (2009). This technique consists of ablating sets of parallel lines in a grid pattern (rastering) across the sample and combining the data into false colour images of individual isotopes. Beam diameters of 15 µm to 25 µm with an ablation depth of approximately 1-2 µm were used in the creation of element maps. Lines were ablated with a repetition rate of 10 Hz, moving horizontally at 15 µm to 25 µm/s, making the effective spatial resolution of each pixel between one and two

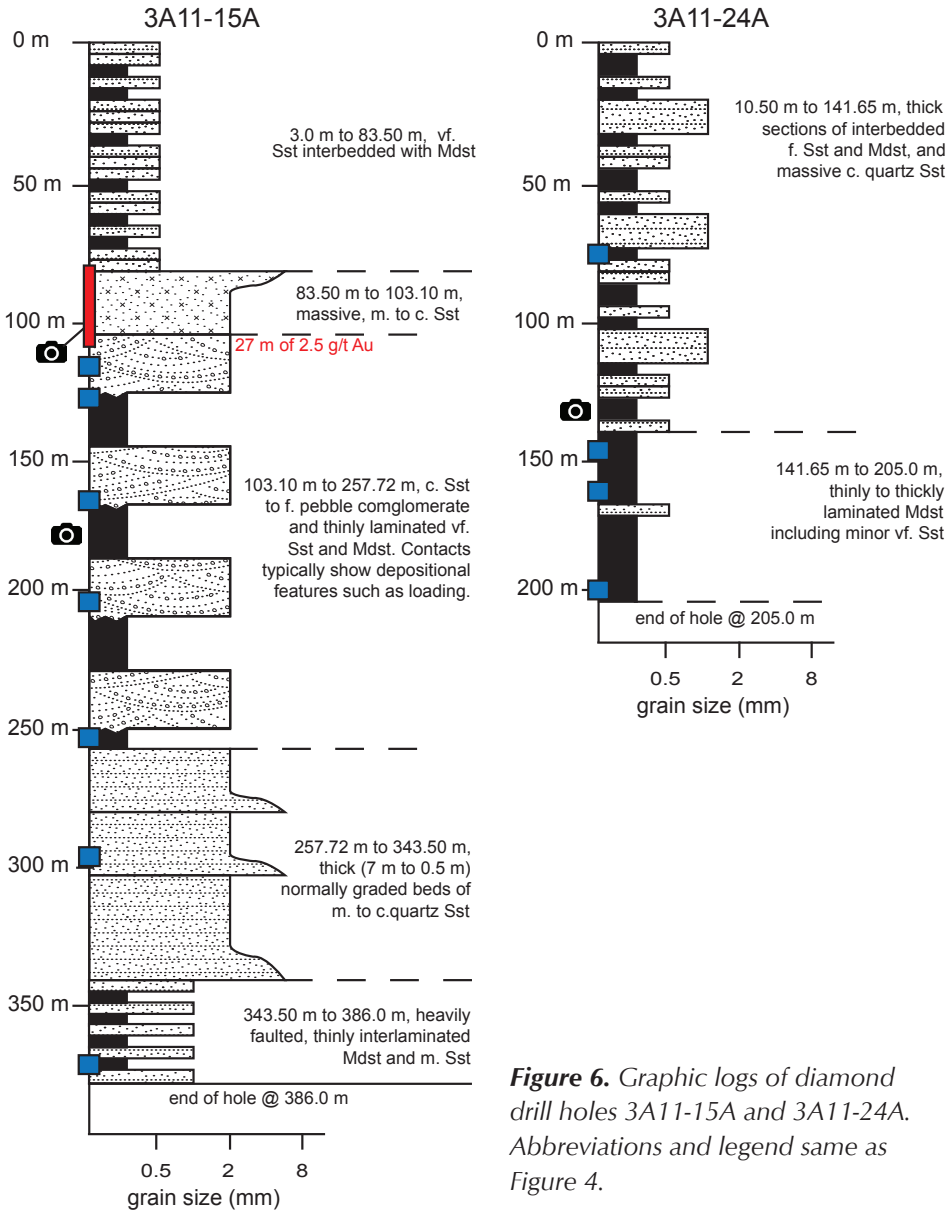

Figure 6. *Graphic logs of diamond drill holes 3A11-15A and 3A11-24A. Abbreviations and legend same as Figure 4.*

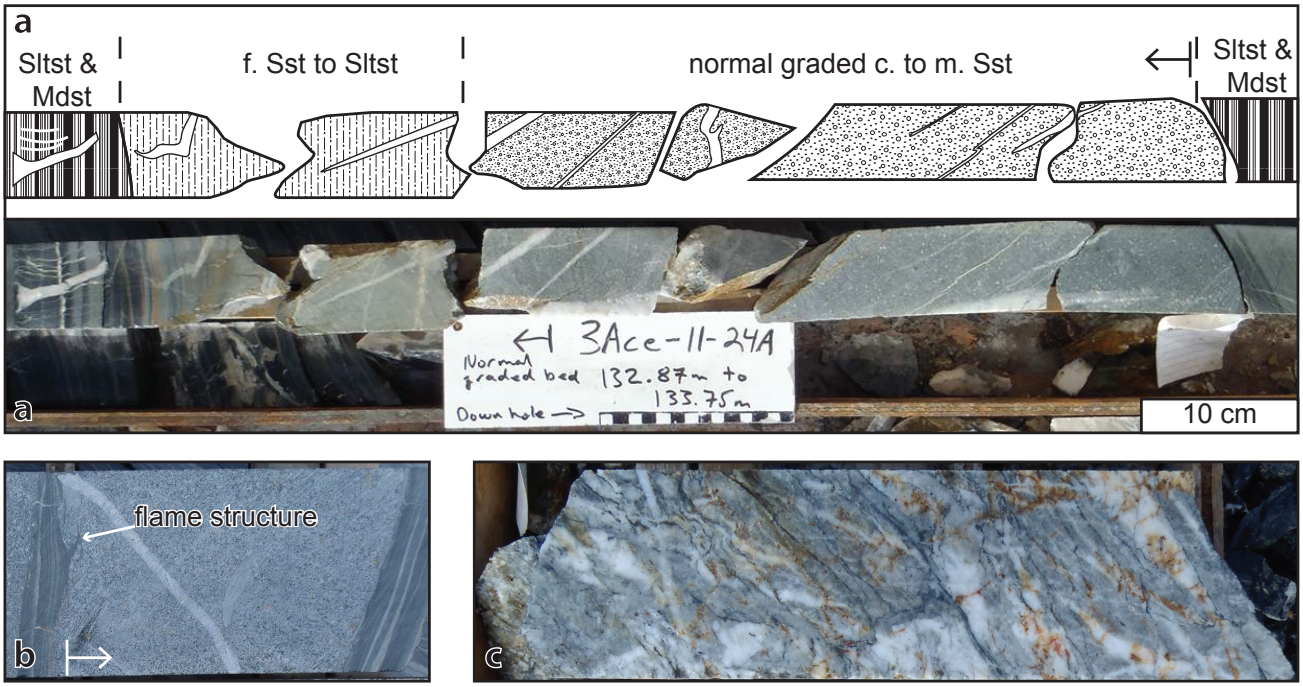

Figure 7. *Representative rocks from the 3Ace occurrence, location of photos shown on Figure 6. (a) 3A11-24A at 133.0m: approximately 1.1 m of core showing a 97 cm graded sandstone bed with mudstone above and below, way-up indicated by flat bottomed arrow. (b) 3A11-15A at 173.67 m: load structures in sandstone and mudstone, way-up indicated by flat bottomed arrow. (c) 3A11-15A at 101.28 m: strongly silicified and quartz veined sample of sandstone in the mineralized interval for this hole. All photos of NQ diamond drill core approximately 5 cm in diameter. Abbreviations same as Figure 4.*

times the beam diameter, depending on the chemical gradient (sharper gradients are easier to see). Processed images are displayed using a logarithmic colour scale corresponding to the signal intensities (counts per second) and not absolute abundance (*e.g.*, ppm). Changes in signal intensities greater than one order of magnitude can be confidently assigned to large changes in element content. Variations smaller than one order of magnitude may reflect subtler variations in element contents.

The calibration standard STDGL2b-2 was used to calculate contents and correct for instrument drift. STDGL2b-2, a certified reference material, is a lithium-borate fused disc of ore concentrate powder doped with certified element solutions (Danyushevsky *et al.*, 2011). Sulphide analyses calibrated on this standard yield an error of less than 15% for most elements. During spot analyses, the standards were analysed twice at the beginning and end of each session, before and after each sample change, and every one to two hours of analysis time. During imaging, the standard was analysed at the beginning and end of data acquisition. Iron was used as an internal standard to correct for differences in laser yield (Danyushevsky *et al.*, 2011). All spot analyses were corrected for linear drift and data reduction was undertaken following the methodology developed by Longerich *et al.* (1996); image data were corrected and reduced according to Large *et al.* (2009). Analyses of Hg concentrations of pyrite cannot be absolutely quantified due to the lack of suitable calibration standards. However, a ratio of Hg to Fe signal intensities can be calculated and used as a measure of relative variations in Hg contents. This ratio acts as a proportional proxy for the Hg content of pyrite. To enable a comparison between Hg/Fe values measured in different analytical sessions, the Hg/Fe values are normalized to Pb/Fe intensity ratios obtained in the same sessions.

RESULTS

PYRITE MORPHOLOGIES

Fine-grained pyrite morphologies (≤50 µm) include sooty microcrystalline aggregates and small anhedra to euhedra (Fig. 8) that are interpreted as having grown early in diagenesis (Large *et al.*, 2007; Raiswell and Plant, 1980). Framboidal pyrite of all sizes is also interpreted as early diagenetic, though under euxinic conditions, fine-grained

syngenetic examples may form within the water column (Large *et al.*, 2007; Raiswell and Plant, 1980; Wilkin *et al.*, 1996). Syngenetic and early diagenetic pyrites contain similar chemical information (Large *et al.*, in press) and for simplicity, we use the term early diagenetic to identify both types. Coarser grained morphologies (>50 µm to 200 µm) include nodular, and large anhedral to euhedral pyrite (Fig. 8) that are interpreted to have formed late in diagenesis at greater depths in the unconsolidated sediments where the nucleation rate is slower (Butler and Rickard, 2000). The formation of these coarser textures may involve some degree of recrystallization (Large *et al.*, 2011). Hydrothermal pyrite from the Conrad occurrence consists mostly of thin (1 µm to 5 µm), arsenian pyrite rims on precursor sedimentary pyrite (Fig. 8), though thicker anhedral to euhedral overgrowths also occur (Tucker *et al.*, 2013). Hydrothermal pyrite from the 3Ace occurrence is generally coarse-grained (>200 µm), and is either associated with quartz veins or as overgrowths on pre-existing sedimentary pyrite (Fig. 8). These four generations

Table 1. *Elements included in the LA-ICP-MS analytical suite. Elements shaded dark grey are used for quality control purposes, elements shaded light grey are primarily found with matrix material or are generally near or below detection in our results (†) and are not discussed. Elements without shading are found primarily within pyrite (focus of this paper). *results for the three isotopes of Pb show similar results, this study uses Pb(206). LA detection limits are a function of spot size, integration duration, and trace element concentration. Detection limits quoted here are mostly the median values calculated for the 31 µm spot size and can be considered a representative average. For full detection limits at all spot sizes used in this study (20 µm, 31 µm, 35 µm, and 50 µm) see the digital Appendices.*

Element (isotope) - 31 µm detection limit in ppm	Element (isotope) - 31 µm detection limit in ppm
Na(23) - 6.22	Mo(95) - 0.021
Mg(24) - 0.104	Ag(107) - 0.022
Al(27) - 0.300	Cd(111) - 0.070
Si(29) - 106	Sn(118) - 0.107
S(34) - 2436	Sb(121) - 0.075
K(39) - 2.61	Te(125) - 0.111
Ca(43) - 116	Ba(137) - 0.02
Ti(49) - 1.26	Gd(157)† - 0.02
V(51) - 0.067	Hf(178)† - 0.009
Cr(53) - 1.18	Ta(181)† - 0.003
Mn(55) - 0.478	W(182) - 0.009
Fe(57) - 5.17	Pt(195)† - 0.01
Co(59) - 0.018	Au(197) - 0.008
Ni(60) - 0.081	Tl(205) - 0.006
Cu(65) - 0.270	Pb(206)* - 0.017
Zn(66) - 0.365	Pb(207)* - 0.021
As(75) - 1.17	Pb(208)* - 0.011
Se(77) - 0.969	Bi(209) - 0.021
Rb(85) - 0.020	Th(232) - 0.004
Sr(88) - 0.003	U(238) - 0.004
Zr(90) - 0.006	

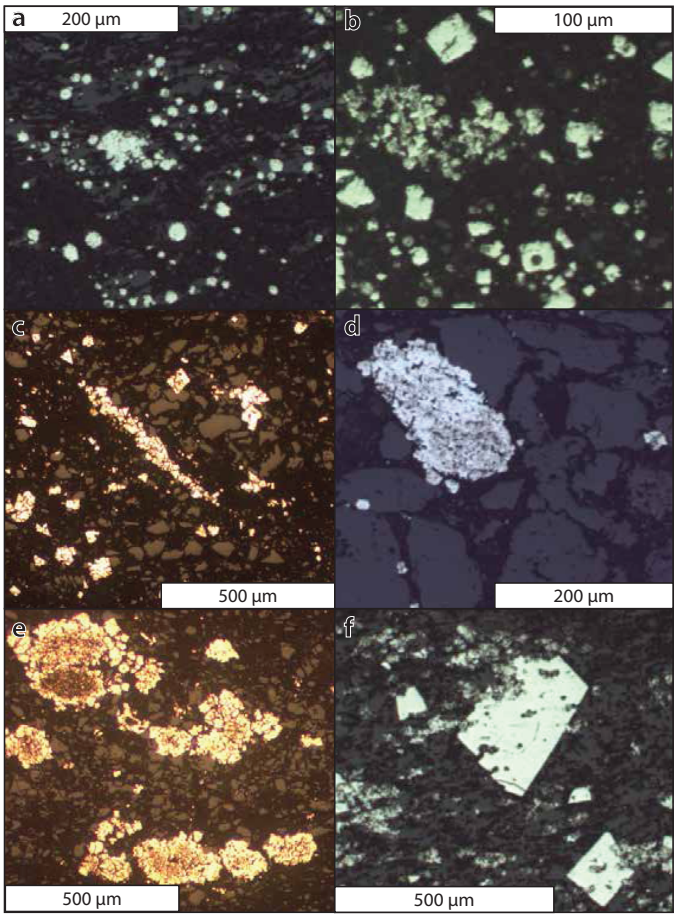

Figure 8. *Reflected light photomicrographs of various pyrite textures. (a) 3A11-24A at 199.30 m: framboidal pyrite. (b) OS11-74 at 76.90 m: early diagenetic fine-grained subhedra to euhedra. (c) OS11-74 at 216.0 m: late diagenetic pyrite nodule and coarse-grained subhedra. (d) OS11-70 at 207.90 m: late diagenetic subhedral pyrite. (e) OS11-70 at 57.25 m: early diagenetic fine-grained sooty microcrystalline core overgrown by cleaner hydrothermal pyrite rim 20 to 30 µm thick. (f) 3A11-15A at 169.97 m: fine-grained diagenetic anhedra overgrown by coarse-grained metamorphic pyrite.*

of pyrite: early diagenetic, late diagenetic, hydrothermal, and vein associated are the textural interpretations upon which our geochemical pyrite characterization are based.

The focus of sampling for this study was on sedimentary pyrite, specifically syngenetic pyrite and diagenetic pyrite; a small number of analyses were done on paragenetically late generations of hydrothermal and vein pyrite (Table 2). Our diagenetic sampling bias does not reflect the relative abundance of pyrite types in the samples, but rather where our analytical interests lie. Nearly half of the pyrite analysed in this study (46%) is fine-grained (≤50 µm) early diagenetic or syngenetic pyrite that occurs as both individual or aggregated framboidal and microcrystalline pyrite. Slightly coarser grained (>50 µm to 200 µm) euhedral to anhedral late diagenetic pyrite, commonly associated with nodules, made up 37% of the analyses. Secondary pyrite, commonly overgrowing diagenetic pyrite, was identified either as thin hydrothermal rims (Conrad) or coarse-grained metamorphic euhedra (3Ace), this population made up 13% of the analyses. A small number of analyses (4%) were done on coarse-grained pyrite associated with veins, but were not studied in detail.

Table 2. *Summary of pyrite morphologies and interpreted paragenesis for each occurrence.*

Pyrite morphology	Paragenetic class	Conrad	3Ace
microcrystalline aggregates, framboidal and small anhedral to subhedral	early diagenetic	47	68
nodular, and large anhedral to euhedral	late diagenetic	56	36
small anhedral overgrowths	hydrothermal	7	26
large euhedral overgrowths			
small to large euhedral	vein	7	2
	Total	**117**	**132**

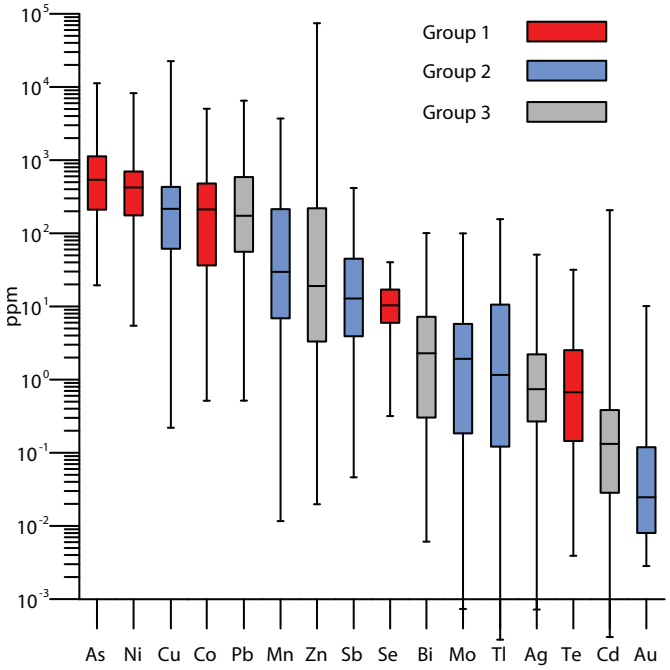

Figure 9. *Range of selected elements using all pyrite data; elements order according to decreasing median values and grouped according to distribution within pyrite as described in the text.*

GENERALITIES OF THE DATA

Data for 41 elements were collected for 249 spot analyses from 22 samples. Twelve of these samples were also image mapped for 41 elements. These data are available digitally in Appendices I and II. The suite of elements collected with the LA-ICP-MS can be broken down into: 1) elements used for internal quality control, 2) elements residing primarily in matrix minerals, and 3) elements primarily associated with pyrite (Table 1). Sulphur and Fe are used for internal quality control purposes, S data are used during processing to ensure results are stoichiometrically feasible for pyrite and Fe is used as the internal standard as described above; these elements are not discussed further. Data from 18 elements that are mostly hosted in matrix, either surrounding pyrite or as inclusions in the pyrite, are used to determine the phase being ablated. When plotted against Al, these matrix associated elements mostly have coefficients of determination (R^2 values) greater than 0.6 (*e.g.*, Na, Mg, Si, K, Ca, V, Cr, Rb, Sr, Zr, Sn, Ba) or are present in concentrations near or below detection limits (*e.g.*, Gd, Hf, Ta, Pt, Th). The remaining 19 elements are associated with pyrite and are the focus of this paper (Table 1).

Following the approach of previous researchers, trace elements are organized according to how they are distributed within pyrite. To accommodate the analytical suite used, the groupings of Huston *et al.* (1995) and Gregory *et al.* (in prep) are modified into the following:

- Group 1 elements (Ni, Co, As, Hg, Se, and Te): stoichiometrically substitute into the lattice of pyrite for Fe and S (Huston *et al.*, 1995), and typically have elevated and consistent LA signals across all element contents.
- Group 2 elements (Cu, Mn, Tl, Sb, Mo, and Au): have consistent LA signals at low element contents where they may be incorporated non-stoichiometrically into the lattice or be held as a uniform distribution of nano-inclusions. At higher element contents, the LA signal for these elements is highly variable, suggesting that they may occur as micro-inclusions (Gregory *et al.*, in prep).
- Group 3 elements (Pb, Zn, Ag, Bi, and Cd): typically have highly variable LA signals at all element contents and are thought to be held primarily within micro-inclusions (Gregory *et al.*, in prep).

Based on the study's entire data set, three generalities are noted. Firstly there are three ranges of trace element data (Fig. 9), in order of decreasing abundance these are: the main trace element constituents of pyrite, As, Ni, Cu, Co, and Pb (typically in the 100s to 1000s ppm range); minor trace element constituents of pyrite, Mn, Zn, Sb, Se, Bi, Mo, Tl, Ag, and Te (typically in the ppm to 10s ppm range); the ultra-trace element constituents of pyrite, Cd and Au, are typically sub-ppm. Secondly, pyrite that is interpreted as early diagenetic has the greatest trace element enrichment, followed by late diagenetic pyrite, hydrothermal, and vein-related pyrite (Fig. 10). Finally, pyrites from the 3Ace occurrence are generally more trace element-rich than those from the Conrad occurrence (Fig. 10).

CONRAD

Eleven samples from the Conrad occurrence were investigated with all four paragenetic classes of pyrite identified and analysed; 103 analyses were done on diagenetic pyrite with seven analyses each on hydrothermal and vein pyrite (Table 2). Besides cursory examination and noting that vein pyrite is depleted in trace elements compared to diagenetic pyrite (Fig. 10), the present study does not examine vein pyrite, and it is not discussed further. Results for elements primarily associated with pyrite are summarized in Table 3.

Early diagenetic and syngenetic pyrites at the Conrad occurrence are typically found as individual or amalgamated framboids or microcrystals; Figure 11 shows early diagenetic pyrite rimmed by hydrothermal pyrite with corresponding select element maps and downhole spectra. Group 1 elements (Ni, Co, As, Hg, Se, and Te) have median values that range from 357 ppm for Ni to 0.4 ppm for Te; Ni has the maximum value of 8347 ppm. The Conrad sedimentary pyrites have very elevated Hg/Fe*1000 ratios, varying from >0.1 to <4.0 with a mean of 0.52 and a median of 0.30. Group 2 elements (Cu, Mn, Tl, Sb, Mo, and Au) have median values that range between 283 ppm for Cu and 20 ppb for Au, Mn has the highest value of 3019 ppm. Group 3 elements (Pb, Zn, Ag, Bi, and Cd) have median values between 174 ppm for Pb and 190 ppb for Cd, Pb also has the maximum value of 2265 ppm.

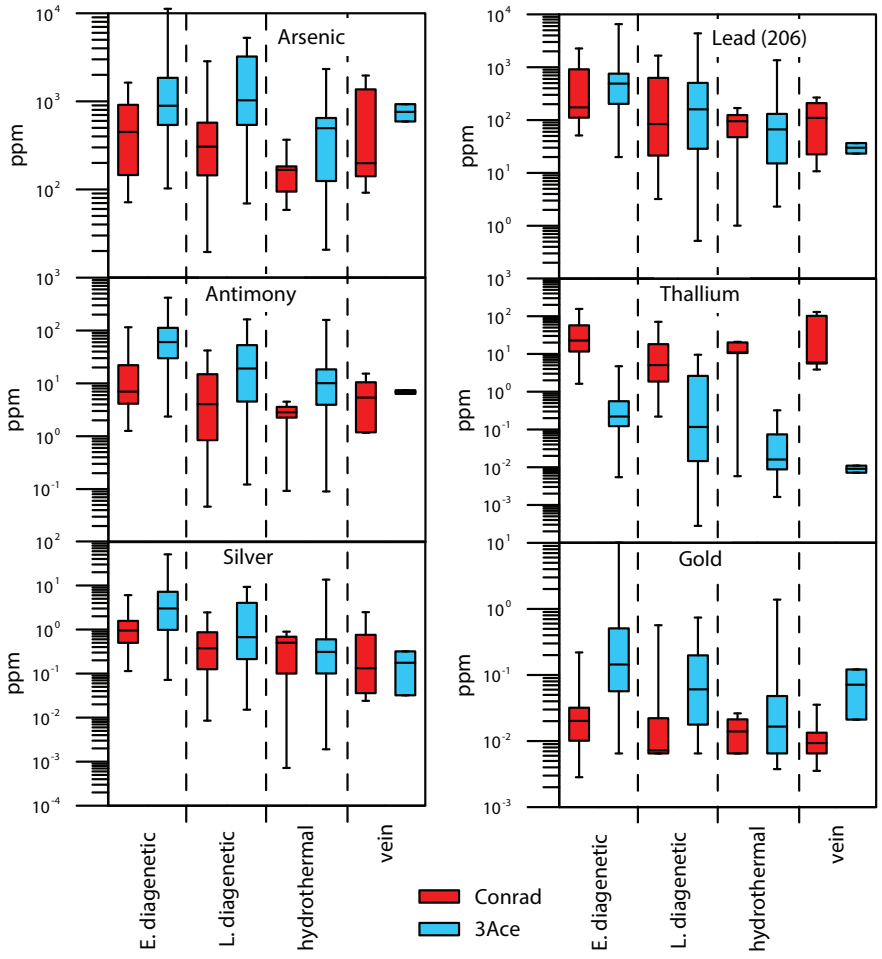

Figure 10. *Box-whisker plots of selected elements showing overall decrease in trace element concentrations between successive generations of pyrite.*

Table 3. *Summary statistics for the Conrad and 3Ace occurrences for elements associated with pyrite. Min. = minimum value, Med. = median value, and Max. = maximum value.*

		Group 1						Group 2						Group 3				
Conrad		**Ni**	**Co**	**As**	**Hg/Fe*1000**	**Se**	**Te**	**Cu**	**Mn**	**Tl**	**Sb**	**Mo**	**Au**	**Pb**	**Zn**	**Bi**	**Ag**	**Cd**
E. diagenetic	Min.	12	3	72	0.014	0.3	0.0	46	1	1.62	1.3	0.07	-0.002	51	2	0.10	0.11	-0.003
	Med.	357	303	449	0.491	7.0	0.4	283	74	22.59	7.0	2.46	0.020	174	26	1.66	0.95	0.190
	Max.	8347	1955	1632	4.051	21.7	5.6	1423	3019	155.95	115.4	63.94	0.219	2265	1116	14.27	6.03	2.211
L. diagenetic	Min.	6	1	19	0.000	0.7	0.0	3	0	0.22	0.0	0.01	-0.003	3	0	0.02	0.01	-0.019
	Med.	179	53	306	0.101	5.7	0.1	150	15	5.09	4.0	0.95	0.007	84	5	0.20	0.37	0.039
	Max.	3224	1162	2851	1.714	32.6	4.4	1689	682	71.03	41.9	25.03	0.566	1657	620	22.27	2.45	1.638
hydrothermal	Min.	6	1	59	0.014	2.7	0.0	16	0	0.01	0.1	0.00	0.000	1	0	0.01	0.00	-0.027
	Med.	106	172	167	0.805	5.2	0.8	247	982	11.23	2.8	2.10	0.014	95	86	1.19	0.50	0.124
	Max.	261	252	367	2.040	18.3	1.5	449	3718	20.96	4.5	3.53	0.026	169	258	2.28	0.89	0.479
3Ace		**Ni**	**Co**	**As**	**Hg/Fe*1000**	**Se**	**Te**	**Cu**	**Mn**	**Tl**	**Sb**	**Mo**	**Au**	**Pb**	**Zn**	**Bi**	**Ag**	**Cd**
E. diagenetic	Min.	170	1	103	-0.010	4.6	0.1	4	5	0.01	2.4	0.03	0.003	20	0	0.44	0.07	-0.330
	Med.	707	339	891	0.022	10.7	2.6	773	327	0.22	60.5	5.92	0.144	490	336	8.09	3.00	0.484
	Max.	2386	5006	11235	0.127	32.5	31.7	22639	3715	4.73	417.6	99.79	10.112	6534	40429	100.68	50.99	29.606
L. diagenetic	Min.	74	10	69	-0.008	8.5	0.0	0	0	-0.01	0.1	-0.03	-0.002	1	-1	0.03	-0.02	-0.326
	Med.	377	251	1028	0.014	18.4	2.5	45	9	0.12	19.1	0.17	0.061	160	8	3.59	0.67	0.086
	Max.	1092	5063	5259	0.075	36.2	19.1	2135	909	9.55	162.5	60.73	0.741	4371	74639	76.29	9.28	207.002
hydrothermal	Min.	47	1	21	-0.006	6.5	0.0	0	0	-0.01	0.1	-0.02	-0.003	2	-1	0.01	0.00	-0.238
	Med.	472	54	496	0.005	15.5	0.6	18	4	0.02	10.1	0.04	0.017	67	3	1.80	0.31	0.023
	Max.	1445	702	2329	0.066	40.4	8.4	10938	546	0.32	158.4	68.76	1.382	1356	32783	44.14	13.57	29.732

Late diagenetic pyrite at the Conrad occurrence is typically coarser grained (50 µm to 200 µm) euhedra to anhedra and the composition is more variable than that of the other paragenetic classes of pyrite. Group 1 elements have median values between 179 ppm for Ni and 0.4 ppm for Te, Ni has the maximum value of 3224 ppm. Group 2 elements median values vary between 150 ppm for Cu and 7 ppb for Au (~detection limit), the maximum value is 1689 ppm for Cu. Group 3 element median values vary between 84 ppm for Pb and 39 ppb for Cd, the maximum value is 1657 ppm for Pb.

Due to the thin (1 µm to 5 µm) rim morphology of most hydrothermal pyrite at the Conrad occurrence (Tucker *et al.*, 2013) only seven analyses were done and these were on ~20 µm thick rims (Fig. 11). Thin rims can be seen in many analyses, but the quality of data obtained from them is too low to be interpreted. The hydrothermal pyrite at the Conrad occurrence is trace element-poor: Group 1 elements have median values between 106 ppm for Ni and 0.8 ppm for Te, maximum value is 261 ppm for Ni; Group 2 median values vary between 982 ppm for Mn and 14 ppb for Au, with 3718 ppm for Mn the maximum value. Group 3 element median values vary between 95 ppm for Pb and 124 ppb for Cd, with a maximum of 258 ppm for Zn.

3ACE

Eleven samples from the 3Ace occurrence were investigated with all four paragenetic types of pyrite analysed; the majority of analyses were done on diagenetic pyrite with 26 analyses of hydrothermal pyrite (Table 2). Two analyses of vein pyrite were also done, but we do not discuss them further. Results for elements primarily associated with pyrite are summarized in Table 3.

Early diagenetic pyrite from the 3Ace occurrence is mostly framboidal; Figure 12 shows early diagenetic pyrite overgrown by hydrothermal pyrite with select element maps and downhole spectra. Group 1 median values vary between 891 ppm for As and 2.6 ppm for Te with 11 235 ppm As the highest value. Hg/Fe*1000 ratios are within the range of normal sedimentary pyrite, varying from <0.004 to 0.13 with a mean of 0.03 and a median of 0.02. Group 2 elements have median values ranging from 773 ppm for Cu to 144 ppb for Au, and a maximum value of 2.2% Cu. Group 3 median values range from 490 ppm for Pb to 484 ppb for Cd, with a maximum value of 4.0% Zn.

Late diagenetic pyrite are mostly 60 µm to 100 µm euhedra or microcrystalline nodules that generally have lower trace element contents than early diagenetic pyrite. Group 1 element median

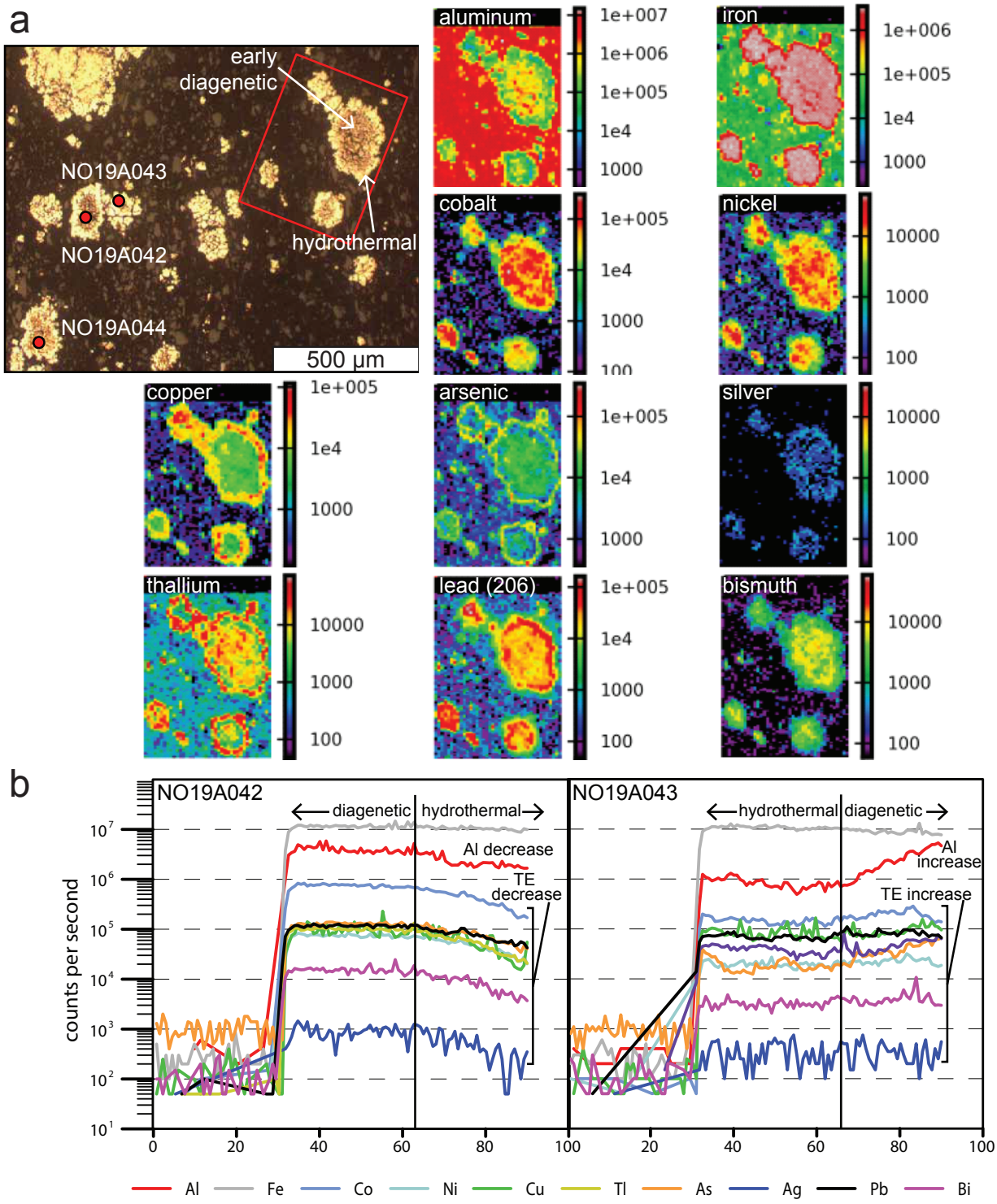

Figure 11. *Representative examples of: (a) element maps; and (b) downhole spectra from OS11-70 at 57.25 m. (a) the red box on the photomicrograph outlines the area mapped using the LA-ICP-MS technique of Large et al. (2009). Selected element maps show distribution of each element within the mapped area. Red circles represent LA-ICP-MS spot ablation sites labelled by analysis number. (b) Selected downhole LA-ICP-MS data for two of the analysis sites shown in a). TE = trace elements.*

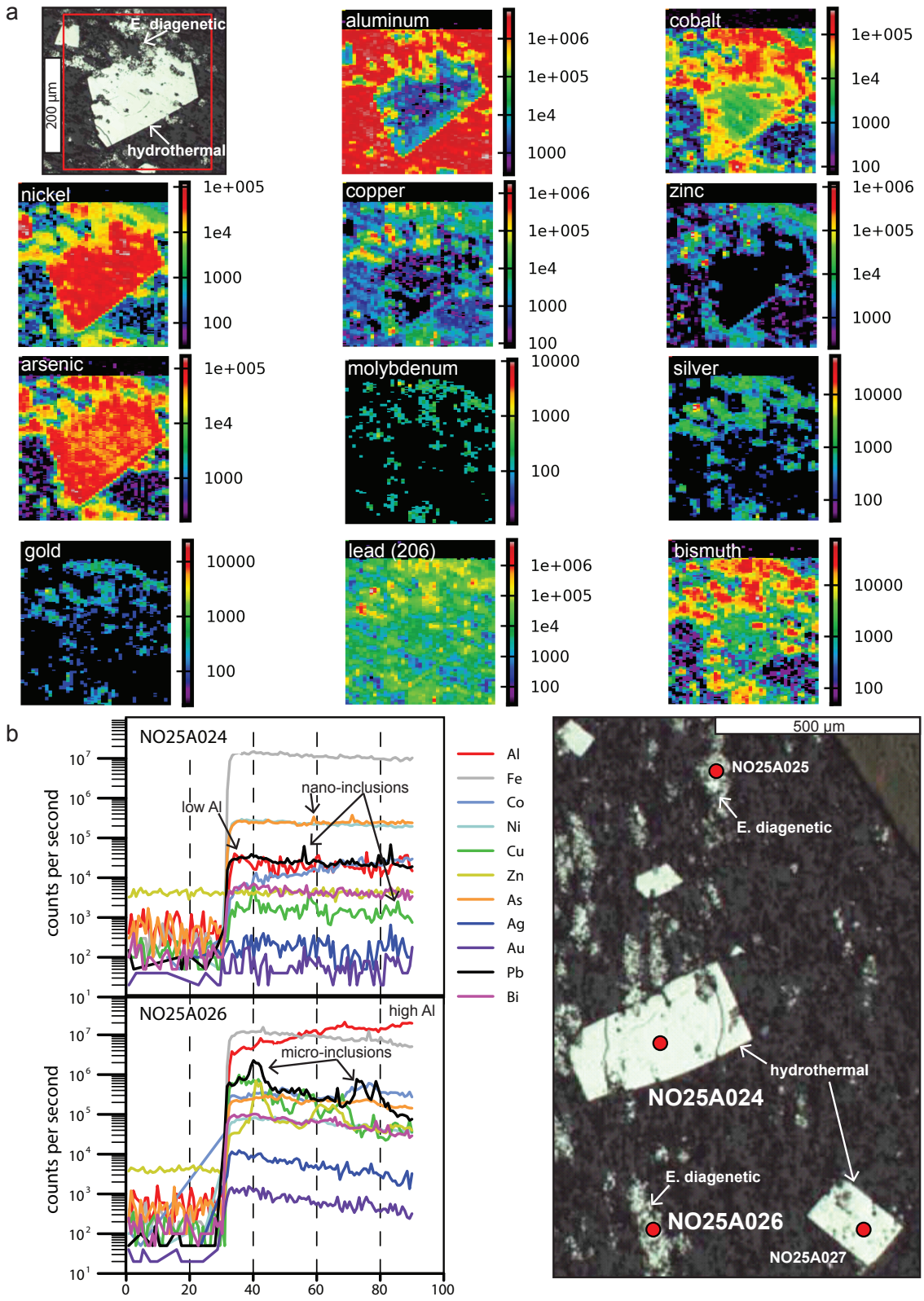

Figure 12. *Representative examples of: (a) element maps; and (b) downhole spectra from 3A11-15A-169.30 m. (a) Red box on the photomicrograph outlines the area mapped using the LA-ICP-MS technique of Large et al. (2009). Selected element maps show distribution of each element within the mapped area. (b) Red circles represent LA-ICP-MS spot ablation sites labelled with the analysis number; selected downhole LA-ICP-MS data for two of the analysis sites are shown.*

values range from 1028 ppm for As to 2.5 ppm for Te, 5259 ppm As is the maximum value. Group 2 elements have median values between 45 ppm for Cu and 61 ppb for Au, reaching a maximum of 2135 ppm Cu. Group 3 elements median values range from 160 ppm for Pb to 86 ppb for Cd, 7.5% Zn is the maximum. Hydrothermal pyrite at 3 Ace is typically coarse-grained (≥200 µm) euhedra overgrowing early diagenetic pyrite. Median values of Group 1 elements range between 496 ppm for As and 0.6 ppm for Te with a maximum value of 2329 ppm As. Group 2 elements have median values between 18 ppm for Cu and 17 ppb for Au, up to a maximum of 1.1% Cu. Group 3 median values range from 67 ppm for Pb to 23 ppb for Cd, with a maximum value of 3.3% Zn.

DISCUSSION

Our samples from the Carlin-type Conrad and orogenic gold 3Ace occurrences are from variably pyritic and calcareous, dark coloured siltstones and mudstones located near the ancient basin to slope transition of Selwyn basin; they are broadly age equivalent with Neoproterozoic (Ediacaran) depositional ages. The Conrad occurrence is hosted by unmetamorphosed mixed carbonate and siliciclastic strata deposited in a continental slope environment, whereas the 3Ace occurrence is hosted entirely within weakly metamorphosed, thick-bedded sequences of siliciclastics likely deposited further into the basin. Our samples share significant similarities (*e.g.*, lithology, age), but they also have significant differences (*e.g.*, depositional facies, style of mineralization, and metamorphic grade).

Ratios of Co/Ni, combined with Ni and Co contents, in pyrite are useful for determining the fluid source for pyrite formation (*e.g.*, Bajwah *et al.*, 1987; Bralia *et al.*, 1979; Clark *et al.*, 2004; Loftus-Hills and Solomon, 1967). Cobalt and Ni are incorporated into the pyrite lattice, and thus these elements are relatively immobile during recrystallization (Huston *et al.*, 1995), retaining their original signature under low intensity hydrothermal and metamorphic conditions, such as those experienced by the samples in our study. Conrad pyrite has a wide range of Ni contents, between 6 ppm and 8347 ppm, but a consistent Co/Ni ratio between 2 and 0.1 (Fig. 13). 3Ace pyrite has consistently high Ni values, mostly between 200 and 2386 ppm, but a wide variation in Co/Ni, ranging from 0.015 in hydrothermal pyrite to 30 in late diagenetic pyrite (Fig. 13). At the Conrad occurrence, the low ratio of Co/Ni suggests a sedimentary fluid source for all generations of pyrite, though the lower Ni content of hydrothermal pyrite may suggest other influences as well (*e.g.*, Campbell and Ethier, 1984; Loftus-Hills and Solomon, 1967). The 3Ace Co and Ni data show a much different pattern with consistently high Ni, but varying Co content (Fig. 13). The preferred explanation for this is that the early diagenetic pyrites at 3Ace, which mostly have Co/Ni values between 2 and 0.1, were formed from sedimentary fluids. The spread in Co data for late diagenetic and hydrothermal pyrite is more ambiguous and may represent an increasing metamorphic or magmatic input but this is poorly understood.

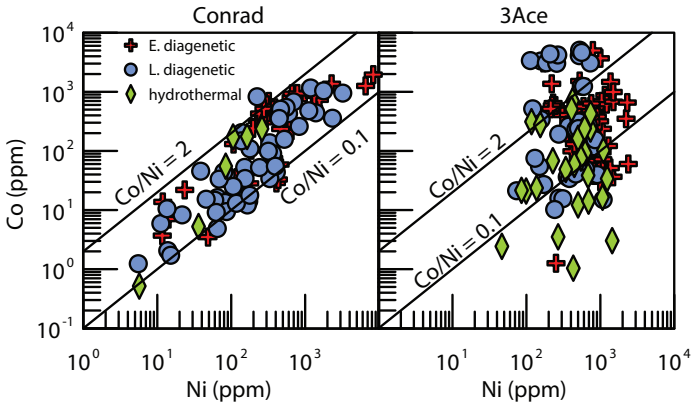

Figure 13. *Ni vs. Co plots of pyrite analyses from Conrad and 3Ace occurrence samples. Co/Ni boundaries from Gregory et al. (in prep).*

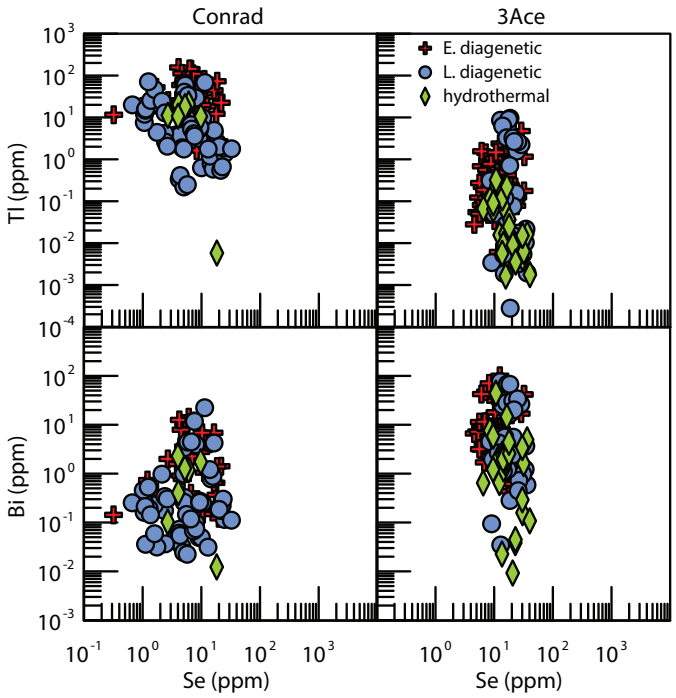

Figure 14. *Se vs. Tl and Bi plots of pyrite analyses from Conrad and 3Ace occurrence samples.*

Thallium is commonly associated with low temperature (<300 °C) hydrothermal fluids associated with syngenetic sulphide deposits (*e.g.*, Gifkins *et al.*, 2005; Goodfellow and Lydon, 2007) and epigenetic gold deposits, such as Carlin-type (*e.g.*, Cline *et al.*, 2005). Bismuth and Te are also associated with hydrothermal fluids, though typically those with higher temperatures (>250 °C), and are common trace elements in orogenic gold systems (Groves *et al.*, 2003). For all stages of pyrite from the Conrad occurrence, elevated Tl in the 1 ppm to >100 ppm and Bi values mostly <1 ppm, (Fig. 14) suggest that hydrothermal fluid temperatures were low through all stages of pyrite formation. Carlin-type deposits form at low temperatures (Cline *et al.*, 2005), and thus this is not an unusual finding for the hydrothermal pyrite. It is uncommon however that the early diagenetic pyrite have such high Tl values (Gregory *et al.*, in prep), up to 156 ppm. These elevated values in early diagenetic pyrite suggest the presence of a synsedimentary hydrothermal fluid. This may support preliminary observations by Gongora and Gleeson (2011) who suggest early, disseminated base metal, sulphide mineralization is present at the Osiris occurrence approximately 2 km to the west of the Conrad. Thallium and Bi levels in pyrite from the 3Ace show an opposite relationship, with 3Ace pyrite typically low in Tl and high in Bi and Te (Fig. 14), which is consistent with mineralization forming at higher temperatures, as would be expected in an orogenic gold deposit.

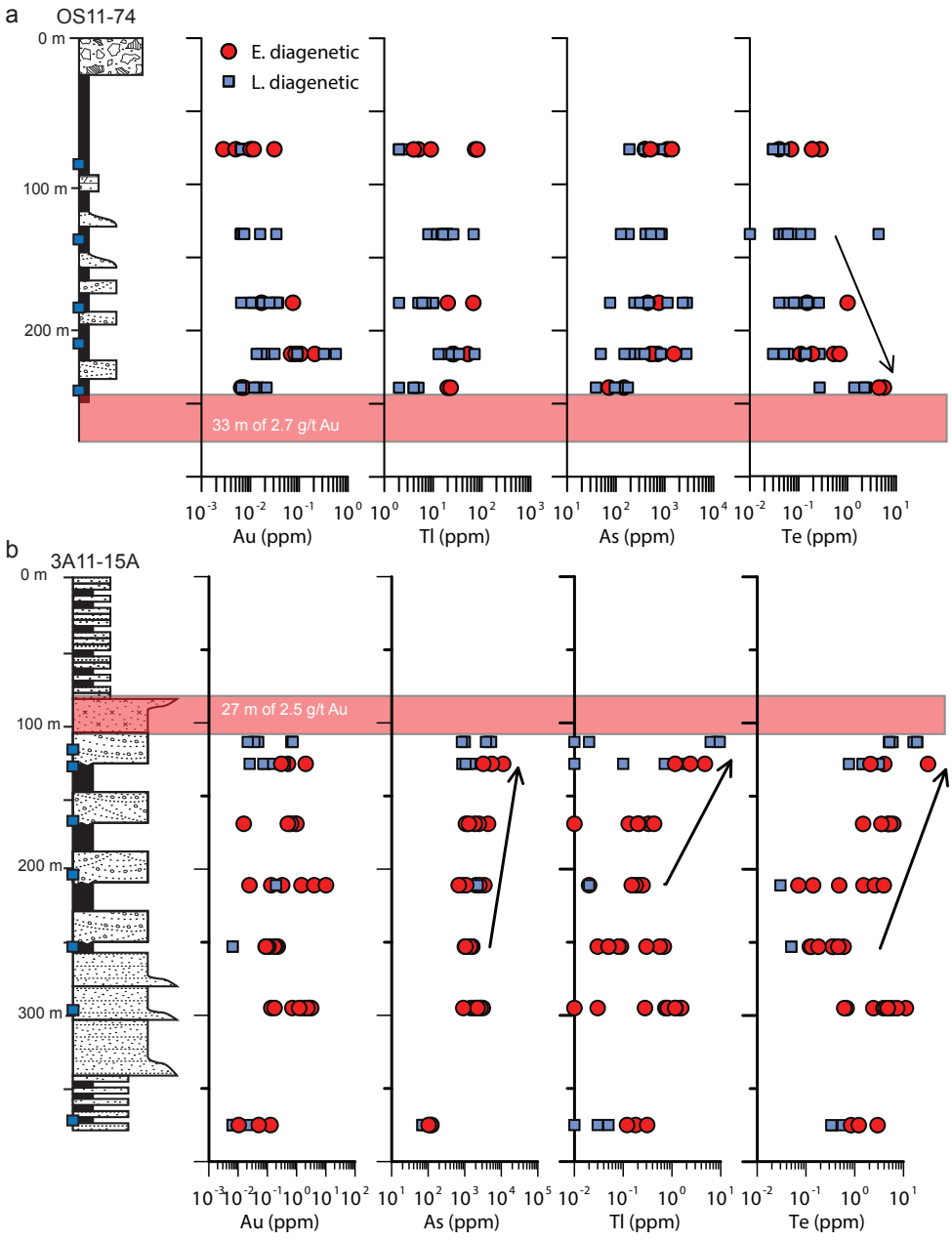

Figure 15. *Downhole plots of selected trace elements for the, (a) Conrad, and (b) 3Ace occurrences. Graphic logs same as in Figure 4 and Figure 6, respectively.*

Preliminary investigation of downhole geochemical vectors in pyrite is inconclusive for the Conrad occurrence where As decreases towards the mineralized interval, Au and Te increase slightly, and Tl remains unchanged (Fig. 15). Mercury is anomalous throughout the stratigraphy surrounding the Conrad occurrence, suggesting that pyrite further from the occurrence is required to determine the full extent of the Hg/Fe*1000 halo and the significance of Hg/Fe as a property-scale vector. In contrast, the downhole pyrite data from 3A11-15A at the 3Ace property show clear property-scale vectors provided by Tl and Te over a drilled length of 100 m to 150 m approaching mineralization (Fig. 15). Arsenic also shows a weak increasing trend over the same interval and Hg/Fe does not show a trend.

COMPARISON WITH OTHER DEPOSITS AND BASINS

The trace element chemistry of sedimentary pyrite has been shown to vary secularly (Large *et al.*, in press), by tectonic setting (Gregory *et al.*, in prep), and by gold productivity of a basin (Large *et al.*, 2011). To simplify comparison between data collected in this study and those from potential analogues, deposits hosted in Neoproterozoic strata deposited near the margin of continental basins have been chosen. Economic Carlin-type deposits are primarily found in slope facies rocks of the Great Basin in Nevada, a similar Neoproterozoic tectonic setting to that of the Conrad occurrence (Arehart *et al.*, 2013), and thus our Conrad pyrite data are best compared to data from some Nevada deposits (*e.g.*, Emsbo *et al.*, 1999; Large *et al.*, 2011; Large *et al.*, 2009). Orogenic gold deposits are found in most orogenic belts; the closest analogue with available pyrite chemistry is the Sukhoi Log gold deposit in eastern Siberia, hosted by continental slope to basinal facies of the Neoproterozoic Patom Group (Large *et al.*, 2007). For a global diagenetic pyrite context, a database compiled at CODES is used, with over 1800 sedimentary pyrite analyses (Large *et al.*, in press). The samples in the Large *et al.* (in press) database range in age from 3600 Ma to present, and are from black shales in both gold productive and unproductive basins. The black shale samples from productive sedimentary basins are distal to known deposits, and show no evidence of hydrothermal alteration. The analyses in this database can be considered representative of background diagenetic pyrite.

Emsbo *et al.* (1999) and Large *et al.* (2009) report the trace element composition of Carlin-type pyrite as having 12 000 ppm to 400 ppm As, 310 ppm to 0.01 ppm Au, and 100s of ppm to <1 ppm of Sb, Tl, Ag, Se, and Te. Conrad data are mostly within these ranges, though a significant number of analyses are below them, with only a few analyses above the preliminary thresholds defined by Large *et al.* (2011; Fig. 16). The Au, As, and Hg/Fe contents of the Conrad diagenetic pyrite are similar to that of distal sedimentary pyrite from the Popovich Formation in the North Carlin Trend (Fig. 16), overlapping with a similar range, but typically having lower median values. Mercury is commonly anomalous in the ore zone and halo of sediment-hosted gold deposits (Boyle, 1979), and recent research by Large (2013) demonstrated that pyrite in the along strike host shales of some of the largest

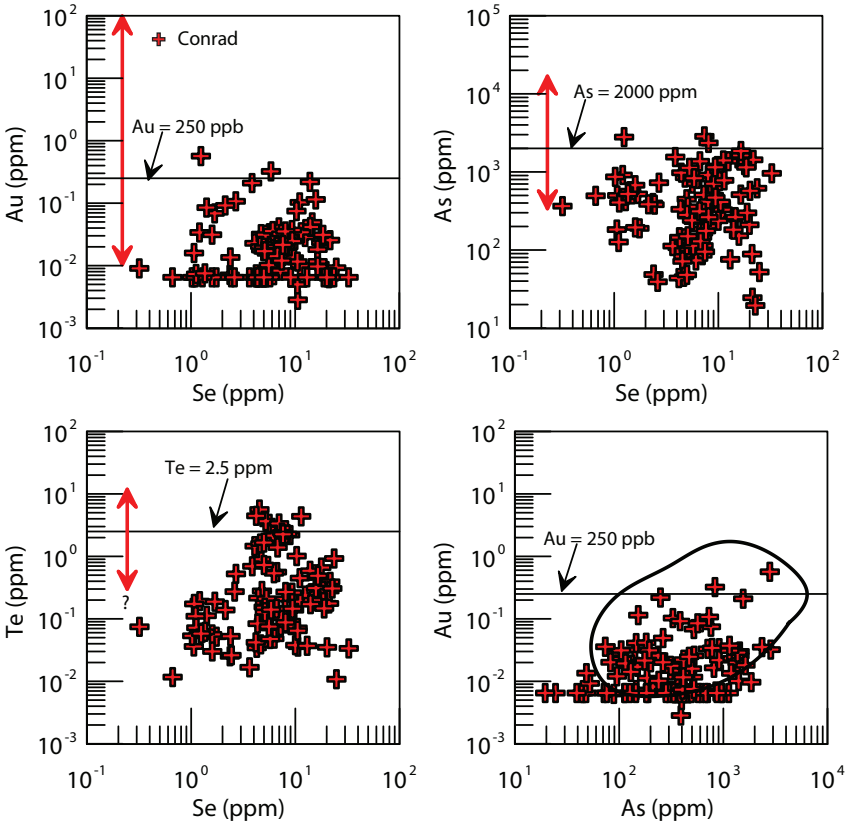

Figure 16. *Diagenetic pyrite (early and late) data for Se vs. Au, As, and Te from the Conrad occurrence and As vs. Au for Conrad with field of distal Popovich Formation diagenetic pyrite from Nevada (Large et al., 2011) outlined in heavy black. Red arrows show the elements range of pyrite from Carlin-type deposits from Emsbo et al. (1999) and Large et al. (2011).*

deposits in the world also contain anomalous levels of Hg. Conrad sedimentary pyrite has a 10 to 20 times larger Hg/Fe ratio than the 3Ace sedimentary pyrite (Fig. 17), and comparison with the Large *et al.* (in press) global database shows that Conrad sedimentary pyrites are at the upper percentile of Hg/Fe*1000 values, with a median of 0.30 (0.11 in the global database). Sedimentary pyrites in black shales from the Popovich Formation of the North Carlin Trend Nevada are the most Hg-rich of those measured in the database, having a median Hg/Fe*1000 value of 0.35. The Hg-enriched diagenetic pyrite at Conrad is a potential regional exploration vector for targeting Carlin-type deposits and prospective host strata. 3Ace pyrite has lower Hg/Fe*1000 values with a median of 0.02 and does not appear to be a regional exploration vector.

Several explanations for the generally low (excluding Hg) trace element content of Conrad diagenetic pyrite are possible: 1) Conrad diagenetic pyrite are trace element-poor compared to those near deposits in Nevada; 2) the upper limit for the ranges of most of the Nevada data is from Emsbo *et al.* (1999), which did not distinguish between generations of pyrite, thus the higher grade analyses may be from ore-stage pyrite; and 3) though the samples for this study were collected from drill holes which contain gold mineralization, they are from intervals that do not carry significant Au grade (Fig. 4). Geochemically, the Conrad sedimentary pyrite appears to be more analogous to the unmineralized, distal Popovich, sedimentary pyrite than sedimentary pyrite collected proximal to the ore shells of deposits.

Large *et al.* (2007) characterize the trace element composition of diagenetic pyrite from Sukhoi Log (referred to as Py1 and Py2) as having Au contents between 13 ppm and 0.002 ppm, and As contents between 13 000 ppm and 159 ppm. The remaining trace elements, Sb, Tl, Ag, and Te range from 175 ppm to <1 ppm (Large *et al.*, 2007). Comparative Se *vs.* Au, As, and Te plots and a Au-As plot show that sedimentary pyrite surrounding Sukhoi Log forms a similar overlapping field to the sedimentary pyrite adjacent to the 3Ace deposit (Fig. 18); approximately 30% of the 3Ace data plots above the preliminary thresholds of Large *et al.* (2011) for Au, As, and Te. Approximately 10% to 30% of the sedimentary pyrite analyses from 3Ace have anomalous chemistry, compared with less than 1% of Conrad analyses (Fig. 19) suggesting that the 3Ace black shales represent a more favourable gold source-rock. This assessment is strengthened by the positive linear relationship between Au-Te and Au-Ag for the sedimentary pyrites at 3Ace (Fig.19). These Au, Te, and Ag correlations in sedimentary pyrite are typical of source rocks that produce moderate to high-grade gold telluride

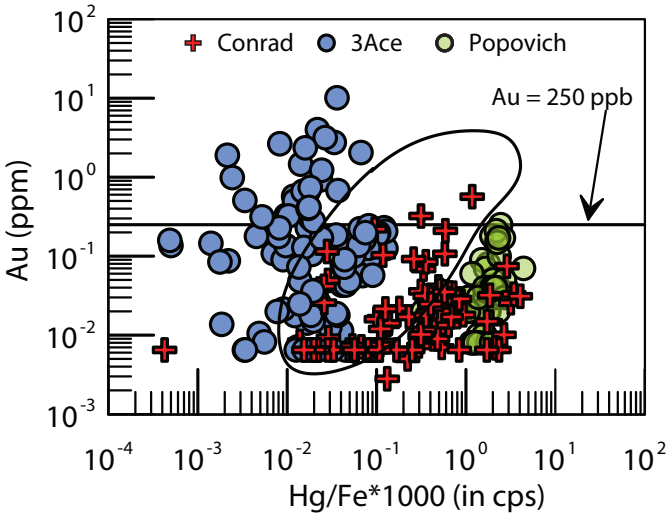

Figure 17. *Hg/Fe*1000 vs. Au plot for Conrad and 3Ace diagenetic pyrite. Distal diagenetic pyrite data from the Popovich Formation in Nevada (Large et al., 2011). Analyses from the sedimentary pyrite database of Large et al. (in press) outlined in black for context. X-axis is a ratio of counts per second (cps), not absolute abundance.*

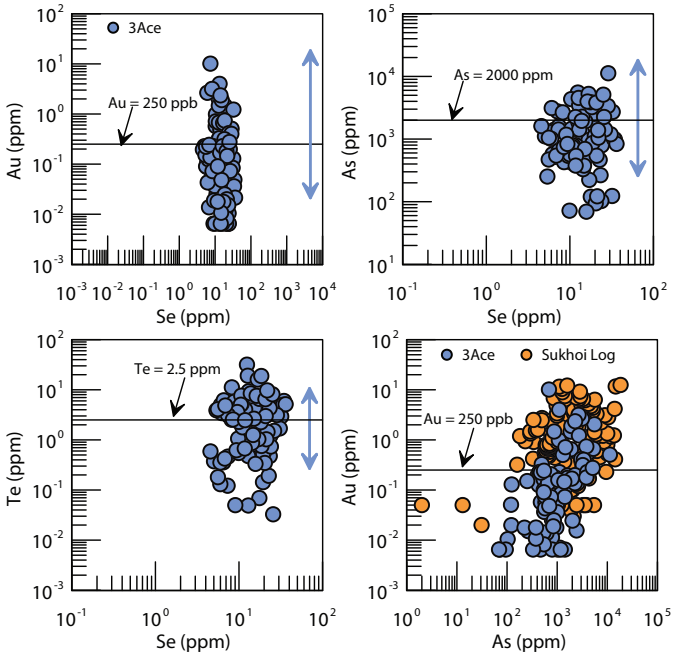

Figure 18. *Diagenetic pyrite (early and late) data for Se vs. Au, As, and Te from the 3Ace occurrence, and As vs. Au for 3Ace diagenetic pyrite and Sukhoi Log diagenetic pyrite. Blue arrow showing the diagenetic pyrite Au, As and Te ranges and Au-As data are from the Sukhoi Log deposit (Large et al., 2007).*

deposits (*e.g.*, Kumtor deposit, Central Asia; Large and Maslennikov, 2011). The Au-Te, Au-Ag plots (Fig. 19), and Te-Bi plot (Fig. 20) show systematic positive trends which suggest that the gold in sedimentary pyrite at both 3Ace and Conrad is present as nano inclusions of Bi-Ag-Au tellurides.

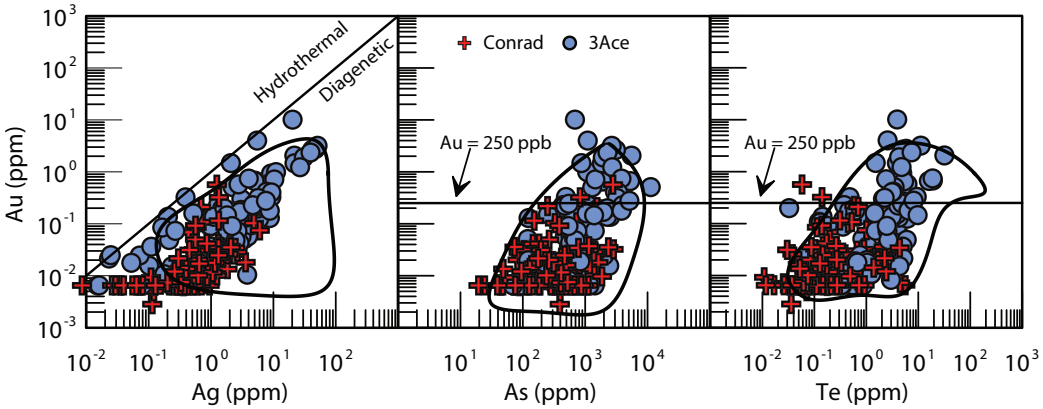

Figure 19. *As, Ag, and Te vs. Au data from Conrad and 3Ace. Analyses from the sedimentary pyrite database of Large et al. (in press) outlined in black for context. Ag vs. Au hydrothermal-sedimentary division from Large et al. (in press), Au = 250 ppb defining potential gold source rocks from Large et al. (2011).*

Large *et al.* (2011) discriminate between gold productive and unproductive basins using data from the Sukhoi Log, Bendigo, and Northern Carlin Trend deposits to represent productive basins and data from the Barney Creek Formation and Rock Cape Group in Australia, and Alum shale in Sweden to represent unproductive basins. There is considerable overlap between these two groups with the division at approximately Au = 250 ppb (Large *et al.*, 2011). On a Au-As plot, diagenetic pyrite from Conrad is mostly confined to the unproductive field whereas approximately 30% of the 3Ace data plots above the 250 ppb Au threshold well into the productive field (Fig. 21). Based on this plot and the overall lower trace element content of the Conrad diagenetic pyrite, it is tempting to infer that the strata around Conrad aren't gold productive. However, the chemistry of the Conrad diagenetic pyrite appears to match quite well with the distal Popovich Formation, diagenetic pyrite of Nevada, which is from within a gold productive basin, and diamond drilling at Conrad has returned some very respectable grades to date indicating significant amounts of Au are present. It appears that gold productive basins have significant amounts of diagenetic pyrite with <250 ppb Au, while unproductive basins rarely have diagenetic pyrite with >250 ppb Au. The diagenetic pyrite data collected suggest the Neoproterozoic stratigraphy of the Selwyn basin area may be productive and that stratigraphy near the 3Ace occurrence has higher Au in diagenetic pyrite than that near the Conrad occurrence.

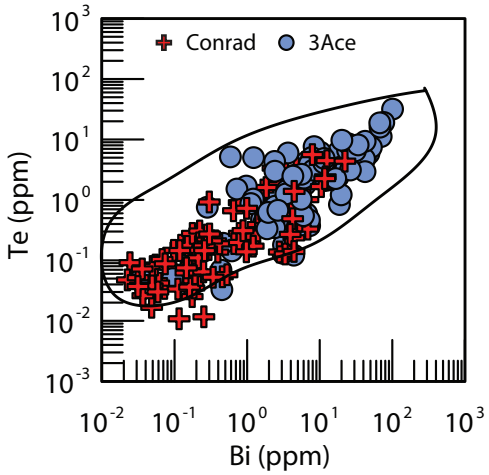

Figure 20. *Bi vs. Te data from Conrad and 3Ace. Analyses from the sedimentary pyrite database of Large et al. (in press) outlined in black for context.*

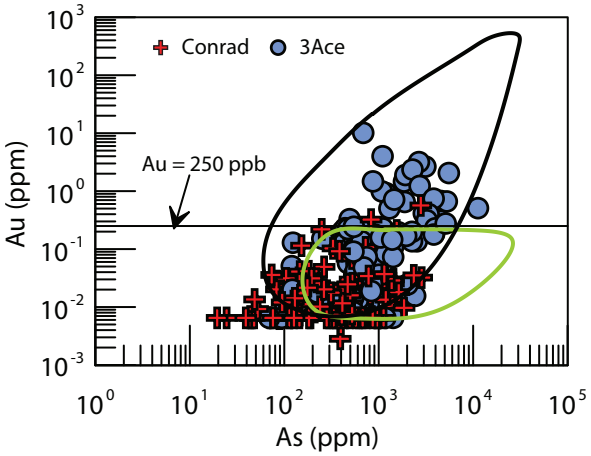

Figure 21. *As vs. Au plot for diagenetic pyrite (early and late) from Conrad and 3Ace occurrences. Productive (black) and unproductive (green) basin fields are from Large et al. (2011).*

CONCLUSIONS

Preliminary observations concerning diagenetic pyrite from two sediment-hosted gold occurrences in the Selwyn basin area are:

CONRAD

- Sedimentary pyrite in the vicinity of the Conrad occurrence has anomalously high Hg (measured as the Hg/Fe ratio by LA-ICP-MS); this elevated Hg content may be a stratigraphic marker for Neoproterozoic stratigraphy favourable for Carlin-like gold deposits in the Selwyn Basin area;
- With the exception of Hg, Conrad diagenetic pyrites are within the lower end of the compositional range of analyses from known Carlin-type deposits, and are more similar to distal sedimentary pyrite from the Popovich Formation in Nevada. The significance of Hg/Fe needs further investigation;
- Elevated Tl, and to a lesser extent Cu and Pb, in early diagenetic pyrite suggest the presence of a synsedimentary hydrothermal fluid near the Conrad occurrence;

3ACE

- At 3Ace the chemistry of sedimentary pyrite appears to be a potential vector to ore over 150 m as highlighted by Te and Tl;
- 3Ace diagenetic pyrite is within the range of analyses from the Sukhoi Log deposit for most trace elements, but is above the range for Te;

OVERALL

- With the exception of Hg, diagenetic pyrite from the Conrad occurrence has lower trace element contents than that from the 3Ace occurrence;
- At both occurrences, early diagenetic pyrite typically has higher trace element contents with successive generations having lower trace element contents;
- Both Conrad and 3Ace sedimentary pyrite show a Bi-Te-Ag-Au relationship indicative of nano particles of gold-bearing bismuth-silver tellurides within the pyrite; and
- Diagenetic pyrite from the Selwyn basin area plot within the field of productive basins on an As vs. Au diagram, but in an area of the diagram that partially overlaps with the unproductive field.

This study characterizes sedimentary pyrite from two of the more prospective sediment-hosted gold occurrences in the Selwyn basin area. The purpose of this characterization is to enable a preliminary comparison between Selwyn basin area sedimentary pyrite and sedimentary pyrite from analogue deposits and basins. This comparison provides an opportunity to apply the Large *et al.* (2011) source-rock model in a truly greenfields setting, as sediment-hosted gold exploration is in its infancy in the Selwyn basin area. Though no economic sediment-hosted gold ore body has been defined in the Selwyn basin area to date, and thus it is not known definitively if the Selwyn basin area is a productive gold basin, the preliminary data suggest that sedimentary pyrite has comparable levels of Au, Te, As, and associated trace elements to known productive basins elsewhere in the world. From this, one can preliminarily conclude that the trace element composition of diagenetic pyrite is permissive of the gold in these occurrences having been sourced, at least in part, locally. That is, the gold in these deposits can be explained using the Large *et al.* (2011) source-rock model. If this model is applicable, then based on the trace element composition of diagenetic pyrite, the Selwyn basin area and Hyland Group stratigraphy, in particular, should be prospective for future sediment-hosted gold exploration.

FURTHER WORK

This study is preliminary in nature and there is much work to be done to further the characterization of sedimentary pyrite and understanding of the significance of pyrite chemistry, both in general and in the Selwyn basin area specifically. Pyrite chemistry as a vector to ore, at both regional and property scales, has only been briefly touched on and several elements appear to be useful. Further study of other elements and relationship of samples to veining and alteration may increase the power of pyrite as a vectoring tool. Arehart *et al.* (2013) describe several other mineral occurrences as sharing similarities with deposits in the Carlin district of Nevada, including the past-producing Brewery Creek mine, which is associated with Cretaceous intrusions, and the Brick-Neve occurrence. Neither of these has been investigated from a Carlin-type perspective and evaluation of the sedimentary pyrite around them could prove interesting. The data collected on sedimentary pyrite do not convincingly demonstrate whether the anomalous Hg at Conrad is a halo effect related to the ore-forming event, or an early Hg-enrichment in pyrite during sedimentation and diagenesis. This important question may be resolved by detailed Pb-isotope measurement of the sedimentary pyrites and hydrothermal pyrites at Conrad. Lastly, this study focussed on diagenetic pyrite at the expense of later pyrite generations, these late generations, particularly those related to mineralization,

may prove interesting, and further study of their chemistry could inform genetic models and possibly add new exploration vectors.

ACKNOWLEDGMENTS

Thank you to ATAC Resources and Northern Tiger Resources for access to their core, education on the property geology, and permission to publish our results. Thank you to Dan Layton-Mathews for reviewing the entire manuscript and to Maurice Colpron and David Moynihan for help with the rapidly changing regional geologic picture. Funding for the analytical portion of this study was provided by the Canadian Northern Economic Development Agency (CanNor) from the Strategic Investment in Northern Economic Development fund (SINED). Finally, the lead author wishes to thank the CODES research group for conducting the analyses, helping with interpretation of results, and contributing to this manuscript.

REFERENCES

Abbott, G., 1997. Geology of the Upper Hart River area, eastern Ogilvie Mountains, Yukon Territory (116A/10, 116A/11). Exploration and Geological Services Division, Department of Indian and Northern Affairs Canada, Bulletin 9, 92 p.

Abbott, J.G., Gordey, S.P., and Tempelman-Kluit, D.J., 1990. Setting of stratiform, sediment-hosted lead-zinc deposits in Yukon and northeastern British Columbia. *In:* Field Trip Guidebook, 8th IAGOD Symposium: Mineral Deposits of the Northern Canadian Cordillera, Yukon-Eastern British Columbia, Abbott, J.G. and Turner, R.J.W. (eds.), Geological Survey of Canada, Open File 2169, p. 69-98.

Arehart, G.B., Ressel, M., Carne, R.C., and Muntean, J., 2013. A comparison of Carlin-type deposits in Nevada and Yukon. *In:* Tectonics, Metallogeny and discovery: The North American Cordillera and similar accretionary setttings, M. Colpron, T. Bissig, B.G. Rusk, and J.F.H. Thompson (eds.), Society of Economic Geologists, Special Publication No. 17, p. 389-401.

Bajwah, Z.U., Seccombe, P.K., and Offler, R., 1987. Trace element distribution, Co:Ni ratios and genesis of the Big Cadia iron-copper deposit, New South Wales, Australia. Mineralium Deposita, vol. 22, p. 292-300.

Blusson, S.L., 1966. Geology, Frances Lake, YukonTerritory and District of Mackenzie. Geological Survey of Canada, Preliminary Map 6-1966, scale 1:253 440.

Boyle, R.W., 1979. The geochemistry of gold and its deposits (together with a chapter on geochemical prospecting for the element). Geological Survey of Canada, GSC Bulletin 280, 584 p.

Bralia, A., Sabatini, G., and Troja, F., 1979. A revaluation of the Co/Ni ratio in pyrite as geochemical tool in ore genesis problems. Mineralium Deposita, vol. 14, p. 353-374.

Buchanan, C. and Oullette, D., 2013. Assessment Report on 2012 Diamond Drilling on the 3Ace Property, Little Hyland River Area, YT., Northern Tiger Resources.

Butler, I.B. and Rickard, D., 2000. Framboidal pyrite formation via the oxidation of iron (II) monosulfide by hydrogen sulphide. Geochimica et Cosmochimica Acta, vol. 64, p. 2665-2672.

Campbell, F.A. and Ethier, V.G., 1984. Nickel and cobalt in pyrrhotite and pyrite from the Faro and Sullivan orebodies. Canadian Mineralogist, vol. 22, p. 503-506.

Cecile, M.P., 2000. Geology of the northeastern Niddery Lake map area, east-central Yukon and adjacent Northwest Territories. Geological Survey of Canada, Bulletin 553, 122 p.

Chakungal, J. and Bennett, V., 2011. New bedrock geology of Mount Mervyn map sheet (106C/04) and mineral potential for the South Wernecke mapping project. *In:* Yukon Exploration and Geology 2010, MacFarlane, K.E., Weston, L.H., and Relf, C. (eds.), Yukon Geological Survey, p. 55-87.

Clark, C., Grguric, B., and Mumm, A.S., 2004. Genetic implications of pyrite chemistry from the Palaeoproterozoic Olary Domain and overlying Neoproterozoic Adelaidean sequences, northeastern South Australia. Ore Geology Reviews, vol. 25, p. 237-257.

Cline, J.S., Hofstra, A., Muntean, J., Tosdal, R., and Hickey, K., 2005. Carlin-type gold deposits in Nevada: Critical geologic characteristics and viable models. *In:* Economic Geology: One Hundreth Anniversary Volume, Hedenquist, J.W., Thompson, J.F.H., Goldfarb, R.J., and Richards, J.P. (eds.), Society of Economic Geologists, p. 451-484.

Colpron, M., 2012. Preliminary observations on the geology of the Rackla belt, Mount Ferrell map-area (NTS 106C/3), central Yukon. *In:* Yukon Exploration and Geology 2011, MacFarlane, K.E. and Sack, P.J. (eds.), Yukon Geological Survey, p. 27-43.

Colpron, M., Moynihan, D., Israel, S., and Abbott, G., 2013. Geological map of the Rackla belt, east-central Yukon (NTS 106C/1-4, 106D/1). Yukon Geological Survey, 5 maps and legend, scale 1:50 000.

Danyushevsky, L., Robinson, P., Gilbert, S., Norman, M., Large, R., McGoldrick, P., and Shelley, M., 2011. Routine quantitative multi-element analysis of sulphide minerals by laser ablation ICP-MS: Standard development and consideration of matrix effects. Geochemistry: Exploration, Environment, Analysis, vol. 11, p. 51-60.

Eisbacher, G.H., 1981. Sedimentary tectonics and glacial record in the Windermere Supergroup, Mackenzie Mountains, northwestern Canada. Geological Survey of Canada, Paper 80-27, 40 p.

Emsbo, P., Hutchinson, R.W., Hofstra, A., Volk, J.A., Bettles, K.H., Baschuk, G.J., and Johnson, C.A., 1999. Syngenetic Au on the Carlin trend: Implications for Carlin-type deposits. Geology, vol. 27, p. 59-62.

Gaboury, D., 2013. Does gold in orogenic deposits come from pyrite in deeply buried carbon-rich sediments?: Insight from volatiles in fluid inclusions. Geology, vol.41, p. 1207-1210.

Gabrielse, H., 1967. Tectonic evolution of the Northern Canadian Cordillera. Canadian Journal of Earth Sciences, vol. 4, p. 271-298.

Gifkins, C., Herrmann, W., and Large, R., 2005. Altered volcanic rocks: A guide to description and interpretation. Centre for Ore Deposit Research (CODES), University of Tasmania, 275 p.

Goldfarb, R.J., Baker, T., Dube, B., Groves, D.I., Hart, C.J.R., and Patrice, G., 2005. Distribution, character, and genesis of gold deposits in metamorphic terranes. *In:* Economic Geology: One Hundredth Anniversary Volume, Hedenquist, J.W., Thompson, J.F.H., Goldfarb, R.J., and Richards, J.P. (eds.), Society of Economic geologists, p. 407-450.

Gongora, P.A. and Gleeson, S.A., 2011. Petrographic and scanning electron microscope study of ore samples from Osiris, Nadaleen Trend, Yukon.

Goodfellow, W.D., 2007. Base metal metallogeny of the Selwyn Basin, Canada. *In:* Mineral Resources of Canada: A Synthesis of Major Deposit-types, District Metallogeny, the Evolution of Geological Provinces, and Exploration Methods, Goodfellow, W. D. (ed.), Mineral Deposits Division, Geological Association of Canada, Special Publication 5, p. 553-579.

Goodfellow, W.D., Cecile, M.P., and Leybourne, M.I., 1995. Geochemistry, petrogenesis, and tectonic setting of lower Paleozoic alkalic and potassic volcanic rocks, Northern Canadian Cordilleran Miogeocline Canadian Journal of Earth Sciences, vol. 32, p. 1236-1254.

Goodfellow, W.D. and Jonasson, I.R., 1987. Environment of formation of the Howards Pass (XY) Zn-Pb deposit, Selwyn Basin, Yukon. *In:* Proceedings Mineral Deposits of Northern Cordillera Symposium, Whitehorse, Yukon, Canada, 1987, Canadian Institute of Mining and Metallurgy, Special Volume 37, p. 19-50.

Goodfellow, W.D. and Lydon, J.W., 2007. Sedimentary exhalative (SEDEX) deposits. *In:* Mineral Deposits of Canada: A synthesis of major deposit types, district metallogeny, the evolution of geological provinces, and exploration methods, Goodfellow, W. D. (ed.), Geological Association of Canada, Special Publication No. 5, p. 163-183.

Gordey, S.P. and Anderson, R.G., 1993. Evolution of the northern Cordilleran miogeocline, Nahanni map area (105I), Yukon and Northwest Territories. Geological Survey of Canada, Memoir 428, 214 p.

Gordey, S.P. and Makepeace, A.J. (comps.), 2001. Bedrock geology, Yukon Territory. Geological Survey of Canada, Open File 3754 and Exploration and Geological Services Division, Yukon Indian and Northern Affairs Canada, Open File 2001-1, scale 1:1 000 000.

Gregory, D., Large, R., Bull, S., Halpin, J., Lounejeva, E., Maslennikov, V.V., Lyons, T., and Sack, P., in prep.

Groves, D.I., Goldfarb, R.J., Gebre-Mariam, M., Hagemann, S.G., and Robert, F., 1998. Orogenic gold deposits: A proposed classification in the context of their crustal distribution and relationship to other gold deposit types. Ore Geology Reviews, vol. 13, p. 7-27.

Groves, D.I., Goldfarb, R.J., Robert, F., and Hart, C.J.R., 2003. Gold deposits in metamorphic belts; overview of current understanding, outstanding problems, future research, and exploration significance. Economic Geology and the Bulletin of the Society of Economic Geologists, vol. 98, p. 1-29.

Hart, C., 2007. Reduced Intrusion-related gold systems. *In:* Mineral Deposits of Canada: A Synthesis of Major Deposit-types, District Metallogeny, the Evolution of Geological Provinces, and Exploration Methods, Goodfellow, W.D. (ed.), Geological Association of Canada, Special Publication 5, p. 95-112.

Hart, C.J.R. and Lewis, L.L., 2006. Gold mineralization in the upper Hyland River area: A nonmagmatic origin. *In:* Yukon Exploration and Geology 2005, D.S. Emond, G.D. Bradshaw, L.L. Lewis, and L.H. Weston (eds.), Yukon Geological Survey, p. 109-125.

Hart, C.J.R., McCoy, D.T., Goldfarb, R.J., Smith, M., Roberts, P., Hulstein, R., Bakke, A.A., and Bundtzen, T.K., 2002. Geology, exploration and discovery in the Tintina Gold Province, Alaska and Yukon. *In:* Global Exploration 2002: Integrated Methods for Discovery, E.E. Marsh, R.J. Goldfarb, and W.C. Day (eds.), Society of Economic Geologists, p. 25-26.

Huston, D.L., Sie, S.H., Suter, G.F., Cooke, D.R., and Both, R.A., 1995. Trace elements in sulfide minerals from eastern Australian volcanic-hosted massive sulfide deposits; Part I, Proton microprobe analyses of pyrite, chalcopyrite, and sphalerite, and Part II, Selenium levels in pyrite; comparison with delta 34 S values and implications for the source of sulfur in volcanogenic hydrothermal systems. Economic Geology, vol. 90, p. 1167-1196.

Lang, J.R. and Baker, T., 2001. Intrusion-related gold systems: the present level of understanding. Mineralium Deposita, vol. 36, p. 477-489.

Large, R., Thomas, H., Craw, D., Henne, A., and Henderson, S., 2012. Diagenetic pyrite as a source for metals in orogenic gold deposits, Otago Schist, New Zealand. New Zealand Journal of Geology and Geophysics, vol. 55, p. 137-149.

Large, R.R., 2013. Orogenic gold deposits through time: A two-stage process. *In:* Proceedings Mines and Wines, Orange, New South Wales, 2013, SMEDG.

Large, R.R., Bull, S.W., and Maslennikov, V.V., 2011. A Carbonaceous Sedimentary Source-Rock Model for Carlin-Type and Orogenic Gold Deposits. Economic Geology, vol. 106, p. 331-358.

Large, R.R., Danyushevsky, L., Hollit, C., Maslennikov, V., Meffre, S., Gilbert, S., Bull, S., Scott, R., Emsbo, P., Thomas, H., Singh, B., and Foster, J., 2009. Gold and trace element zonation in pyrite using a laser imaging technique: Implications for the timing of gold in orogenic and Carlin-style sediment-hosted deposits. Economic Geology, vol. 104, p. 635-668.

Large, R.R., Halpin, J.A., Danyushevsky, L.V., Maslennikov, V.V., Bull, S.W., Long, J.A., Gregory, D.D., Lounejeva, E., Lyons, T.W., Sack, P.J., McGoldrick, P., and Calver, C.R., in press. Trace element content of sedimentary pyrite as a new proxy for deep-time ocean-atmosphere evolution. Earth and Planetary Science Letters.

Large, R.R. and Maslennikov, V., 2011. Pyrite textures, composition and isotopic features at the Kumtor gold deposit, Kyrgyzstan: New data to improve the genetic model. *In:* Conference Proceedings, Society for Geology of Ore Deposits, Antofagasta, Chile, 2011, SGA.

Large, R.R., Maslennikov, V.V., Robert, F., Danyushevsky, L.V., and Chang, Z., 2007. Multistage sedimentary and metamorphic origin of pyrite and gold in the giant Sukhoi Log deposit, Lena Gold Province, Russia. Economic Geology, vol. 102, p. 1233-1267.

Loftus-Hills, G. and Solomon, M., 1967. Cobalt, nickel and selenium in sulphides as indicators of ore genesis. Mineralium Deposita, vol. 2, p. 228-242.

Longerich, H.P., Jackson, S.E., and Gunther, D., 1996. Laser ablation inductively coupled plasma-mass spectrometric transient signal data acquisition and analyte concentration calculation. Journal Analytical Atomic Spectrometry, vol. 11, p. 899-904.

Lydon, J.W., Lancaster, R.D., and Karkkainen, P., 1979. Genetic controls of Selwyn Basin stratiform barite/sphalerite/galena deposits; an investigation of the dominant barium mineralogy of the Tea Deposit, Yukon, Current Research, Part B. Geological Survey of Canada, Paper 79-1B, p. 223-229.

Medig, K.P.R., Thorkelson, D.J., Turner, E.C., Davis, W.J., Gibson, H.D., Rainbird, R.H., and Marshall, D.D., 2012. The Proterozoic Pinguicula Group, Wernecke Mountains, Yukon: A siliciclastic and carbonate slope to basin succession with local and exotic sediment provenance. *In:* Yukon Exploration and Geology 2011, K.E. MacFarlane and P.J. Sack (eds.), Yukon Geological Survey, p. 129-149.

Moynihan, D.P., 2013. A preliminary assessment of low pressure, amphibolite-facies metamorphism in the upper Hyland River area (NTS 105H), southeast Yukon. *In:* Yukon Exploration and Geology 2012, K.E. MacFarlane, M.G. Nordling, and P.J. Sack (eds.), Yukon Geological Survey, p. 99-114.

Moynihan, D.P., 2014 (this volume). Bedrock Geology of NTS 106B/4, Eastern Rackla Belt. *In:* Yukon Exploration and Geology 2013, K.E. MacFarlane, M.G. Nordling, and P.J. Sack (eds.), Yukon Geological Survey, p. 147-167.

Nelson, J.L., Colpron, M., and Israel, S., 2013. The Cordillera of British Columbia, Yukon, and Alaska: Tectonics and metallogeny. *In:* Tectonics, Metallogeny and discovery: The North American Cordillera and similar accretionary setttings, M. Colpron, T. Bissig, B.G. Rusk, and J.F.H. Thompson (eds.), Society of Economic Geologists, Special Publication No. 17, p. 53-109.

Pigage, L.C., 1990. Field guide Anvil Pb-Zn-Ag district Yukon Territory, Canada. *In:* Field Trip Guidebook, 8th IAGOD Symposium: Mineral Deposits of the Northern Canadian Cordillera, Yukon-Eastern British Columbia, J.G. Abbott and R.J.W. Turner (eds.), Geological Survey of Canada, Open File 2169, p. 283-308.

Raiswell, R. and Plant, J., 1980. The incorporation of trace elements into pyrite during diagenesis of black shales, Yorkshire, England. Economic Geology, vol. 75, p. 684-699.

Read, P.B., Woodsworth, G.J., Greenwood, H.J., Ghent, E.D., and Evenchick, C.A., 1991. Metamorphic map of the Canadian Cordillera.Geological Survey of Canada, Map 1714A, scale 1:2 000 000.

Sack, P.J., Danyushevsky, L.V., Gilbert, S.E., Large, R., and Gregory, D., 2013. Diagenetic pyrite, a source of gold in sediment-hosted gold deposits? Examples from the Selwyn basin, Yukon. *In:* Proceedings GAC-MAC Winnipeg 2013, Geological Association of Canada, vol. 36, p. 173.

Thorkelson, D.J., Mortensen, J.K., Creaser, R.A., Davidson, G.J., and Abbott, J.G., 2001. Early Proterozoic magmatism in Yukon, Canada: constraints on the evolution of northwestern Laurentia. Canadian Journal of Earth Sciences, vol. 38, p. 1479-1494.

Tucker, M.J., Hart, C.J.R., and Carne, R.C., 2013. Geology, alteration, and mineralization of the Carlin-type Conrad zone, Yukon. *In:* Yukon Exploration and Geology 2012, K.E. MacFarlane, M.G. Nordling, and P.J. Sack (eds.), Yukon Geological Survey, p. 163-178.

Turner, E.C. and Long, D.G.F., 2008. Basin architecture and syndepositional fault activity during deposition of the Neoproterozoic Mackenzie Mountains supergroup, Northwest Territories, Canada. Canadian Journal of Earth Sciences, vol. 45, p. 1159-1184.

Wheeler, J.O. and McFeely, P., 1991. Tectonic assemblage map of the Canadian Cordillera and adjacent parts of the United States of America. Geological Survey of Canada, Map 1712A, scale 1:2 000 000.

Whelan, S.C., Gleeson, S.A., Stern, R.A., and Buchanan, C., 2013. Au mineralization at 3Ace, south-east Yukon. *In:* Proceedings GAC-MAC Winnipeg 2013, Geological Association of Canada, vol. 36, p. 197.

Wilkin, R., Barnes, H., and Brantley, S., 1996. The size distribution of framboidal pyrite in modern sediments: An indicator of redox conditions. Geochimica et Cosmochimica Acta, vol. 60, p. 3897-3912.